

4-1-91  
E6049

NASA Technical Memorandum 103778

# Development of a Laser-Induced Heat Flux Technique for Measurement of Convective Heat Transfer Coefficients in a Supersonic Flowfield

A. Robert Porro  
*Lewis Research Center*  
*Cleveland, Ohio*

Theo G. Keith, Jr.  
*University of Toledo*  
*Toledo, Ohio*

and

Warren R. Hingst, Randall M. Chriss and Kirk D. Seablom  
*Lewis Research Center*  
*Cleveland, Ohio*

March 1991

**NASA**

# Table of Contents

|   |     |
|---|-----|
| Nomenclature . . . . .  | iii |
| Chapter 1. Introduction . . . . .   | 1   |
| 1.1. Origin and Importance of the Investigation . . . . .                   | 1   |
| 1.2. Survey of Convective Heat Transfer Measurement<br>Techniques . . . . . | 2   |
| 1.3. Objective of the Investigation . . . . .                               | 4   |
| Chapter 2. Experimental Apparatus and Technique . . . . .                   | 6   |
| 2.1. Laser-Induced Heat Flux Apparatus . . . . .                            | 6   |
| 2.2. Wind Tunnel Facility . . . . .   | 8   |
| 2.3. Wind Tunnel Model . . . . .  | 9   |
| 2.4. Experimental Technique . . . . .                                       | 11  |
| 2.4.1. LIHF System Calibration . . . . .                                    | 11  |
| 2.4.2. Experimental Method . . . . .  | 13  |
| Chapter 3. Analysis . . . . .   | 15  |
| 3.1. Data Reduction . . . . .   | 15  |
| 3.2. Heat Transfer Analysis . . . . .                                       | 16  |
| Chapter 4. Results and Discussion . . . . .                                 | 19  |
| 4.1. Flow Surface Thermal Images . . . . .                                  | 19  |
| 4.2. Static Pressure Measurements . . . . .                                 | 22  |
| 4.3. Local Mach Number Distributions . . . . .                              | 23  |
| 4.4. Heat Transfer Measurements . . . . .                                   | 25  |
| 4.4.1. LIHF System Temperature Calibration . . . . .                        | 25  |

|                        |   |    |
|------------------------|---|----|
| 4.4.2.                 | Experimental Convective Heat Transfer Coefficients and Comparison with Theory . . . . . | 26 |
| Chapter 5.             | Concluding Remarks . . . . .  | 31 |
| Bibliography . . . . . |   | 33 |
| Appendix A.            | Thermodynamic and Isentropic Relations . . . . .  | 36 |
| Appendix B.            | Estimation of Static Pressure and Mach Number Uncertainty . . . . .                     | 38 |
| Appendix C.            | Estimation of Convective Heat Transfer Coefficient Uncertainty . . . . .                | 39 |

## Nomenclature

|          |  |
|----------|--|
| A        | heated area due to applied heat flux, $2\pi r\delta$                           |
| h        | convective heat transfer coefficient ( $W/m^2K$ )                              |
| $I_0$    | modified Bessel function of the first kind of order 0                          |
| $K_0$    | modified Bessel function of the second kind of order 0                         |
| $K_1$    | modified Bessel function of the second kind of order 1                         |
| k        | thermal conductivity of gel-coat resin ( $0.519 W/m^2K$ )                      |
| L        | flat plate model length, 40.64 cm  |
| M        | Mach number  |
| P        | static pressure (Pa)   |
| $P_o$    | total or pitot pressure (Pa)   |
| $P_r$    | reflected laser power (W)  |
| $P_t$    | transmitted source laser power (W)   |
| Pr       | Prandtl number   |
| q        | heat transfer rate (W)   |
| Re       | Reynolds number  |
| r        | refers to radial distance of heated area element                               |
| $r_c$    | wall temperature recovery factor   |
| $r_s$    | radius of applied laser source, 0.65 mm  |
| S        | flat plate model width, 30.48 cm   |
| St       | Stanton number   |
| T        | static temperature (K)   |
| $T_o$    | total temperature (K)  |
| $T_w$    | local wall temperature (K)   |
| x        | axial (streamwise) coordinate relative to leading edge of the flat plate model |
| z        | width (spanwise) coordinate relative to model centerline                       |
| $\delta$ | nominal thickness of gel-coal resin, 1 mm                                      |
| $\theta$ | reference temperature, $T - T_{aw}$  |

## Subscripts

|    |                                      |
|----|--------------------------------------|
| aw | refers to adiabatic wall condition   |
| o  | refers to total or plenum conditions |
| r  | refers to radial position            |

# Chapter 1 Introduction

## 1.1. Origin and Importance of the Investigation

Current efforts in aerospace research and development are aimed towards high speed flight. The National Aerospace Plane Program (NASP) is developing an aircraft that can take off from a conventional runway and accelerate to a low earth orbit trajectory. This aircraft will cover the speed regime from Mach 0 to 25. Also, NASA is initiating a research program to develop basic technology needed for a High Speed Civil Transport (HSCT). The HSCT is projected to have a top speed of Mach 5.

Associated with high Mach number flight is increased aerodynamic heating and the need for an aircraft designer to foresee potential heating problem areas while the aircraft concept is in the design stage. For example, consider the case of NASA's X-15 hypersonic research aircraft. A serious heat transfer problem occurred on its last research flight. A dummy hypersonic ramjet engine was mounted on the ventral fin of the X-15. On this test flight, the aircraft achieved its highest speed ever, Mach 6.70. However, a focussing of shock waves on the ventral fin which emanated from the ramjet burned through the fin's material. This resulted in substantial damage to the aircraft's superstructure and to subsystems enclosed in the ventral fin. Before the damage could be repaired, the X-15 test program was cancelled. The damage due to the shock impingement was a total surprise to the researchers.

This illustration demonstrates the urgent need to be able to predict aerodynamic heat transfer characteristics while an aircraft is being designed. In order to accomplish this, reliable heat transfer data must be obtained through basic wind tunnel experiments that consider aerothermal problems such as shock/boundary layer interactions and stagnation point heat transfer.

In the NASP program, there is a major effort underway to develop an understanding of the internal flow physics associated with high speed aircraft inlets. From

these studies, it has been determined that one of the most critical requirements for the design of a NASP inlet system is the possession of knowledge regarding the surface heating rates. Since it is difficult to obtain experimental heat transfer data at flight conditions, computational fluid dynamics analysis is being used to augment the insufficient heat transfer database. Fundamental experimental heat transfer data must be obtained in order to verify the accuracy of these CFD techniques.

## **1.2. Survey of Convective Heat Transfer Measurement Techniques**

The convective heat transfer coefficient is a parameter which may be used to quantify the heat transfer that occurs as a result of a fluid passing over a solid surface when a convective heat exchange takes place. In an experiment, the quantities measured usually are the model surface heat flux and the temperature. Fundamental relationships that depend on the fluid flow regime are used to relate these measured quantities to the convective heat transfer coefficient.

A standard measurement technique that has been used for some thirty years is the surface-mounted heat flux gauge. As the name implies, the gauge is flush mounted on the surface of the model. It senses both the wall heat flux and the temperature, and hence, the convective heat transfer coefficient. The original surface heat flux gauge is the Gardon gauge and is still widely used in heat transfer measurements [1]. In recent years, variations of the Gardon gauge have been successfully used in making heat transfer measurements. Hayashi et al. [2] have developed a high response surface heat flux gauge with good spatial resolution that has been used to measure convective heat transfer at a shock wave/ turbulent boundary layer interaction.

These surface-mounted heat flux gauges have the advantage of being compact; typically they are on the order of 1 mm in diameter. This small size insures that the temperature gradient created by the local heat flux through the gauge does not affect the gross convective heat transfer of a model surface. Since the gauges are flush mounted on the surface, they are non-intrusive, i.e., they do not disturb the incoming

fluid flow. However, a major disadvantage in using this measurement technique is that the gauges have to be permanently mounted on a model. This limits the region where heat transfer measurements can be made, especially in areas where model geometries are complicated.

A method used by researchers to determine the local convective heat transfer coefficient in high speed compressible flows uses a thin metallic plate instrumented with high response thermocouples [3][4][5][6]. The technique is a transient method which monitors the time rate of change of the temperature indicated by each thermocouple. In a typical experiment, the wind tunnel is brought online, and the model is injected into the flow for a short duration during which the transient temperature distribution is monitored. A local heat transfer coefficient is computed at each thermocouple location by using a thin skin energy balance that considers the time rate of temperature change.

One disadvantage of the technique is that it can only be applied to a situation where the model is exposed to the flowfield for a short duration, typically on the order of seconds. This requires the use of a model injection system which is not available at all wind tunnel facilities. Another problem encountered is that the measurement technique requires the use of models with very thin surface thicknesses. The models used in Refs. [3-6] were approximately 0.8 mm thick. In applications where high local surface heating rates were encountered, the thin models suffered surface warping which resulted in permanent model damage [6].

Another convective heat transfer measurement technique uses electrically heated, surface mounted metallic strips instrumented with thermocouples [7][8][9][10]. Since the heat flux due to the joule heating and surface temperatures are known, an average heat transfer coefficient can be calculated. A disadvantage with this technique is that the heat flux is usually applied only over a discrete portion of the model, so the boundary conditions at the unheated/heated interface must be accounted for in order to properly interpret the heat transfer data.

A technique that has been used recently uses a composite of a heated metallic element and liquid crystals to determine the local surface convective heat transfer [11][12]. A thin, conducting metallic layer is bonded to the test surface. Next, a thin layer of liquid crystals is bonded to the metallic layer. The liquid crystal, by virtue of its color change properties, provides a measurement of the local temperature and a visualization of thermal patterns. As before, the heated metallic strip provides the known heat flux. Care must be taken to document the uniformity of the metallic layer, since the local heat flux will vary with film thickness. The model surface to which the composite is bonded must be protected because any exposure of the liquid crystal to the atmosphere will ruin the integrity of the composite coating.

Carlomagno et al. [13] used the joule heating approach (electrically heated thin metallic strips) to induce a heat flux at a model surface, but instead of using thermocouples, the model surface temperatures were monitored by infrared thermography. The advantage in using infrared thermography is that the technique is non-intrusive, and conduction errors inherent to the use of thermocouples are eliminated.

Heath et al. [14] also used infrared thermography to monitor surface model temperatures, but a laser was used to induce a linear heat flux over a large model surface area. With the use of the laser to induce a heat flux, a variety of approaches can be used to analyze the data. The approach taken by Heath et al. monitors the time rate of decay of temperature after the model surface was heated. This method yields only the heat transfer coefficient relative to a natural convection heat transfer coefficient.

### **1.3. Objective of the Investigation**

The primary objective of this investigation is to develop a practical instrumentation system capable of high resolution surface convective heat transfer measurements in complex, three-dimensional high speed flows. Ideally, such a technique should be non-intrusive so that the flowfield surrounding a model is not disturbed at all by

the measurement apparatus. Also, it is desirable for the measurements to be made efficiently at multiple locations on a model surface during the same test run.

In order to satisfy these objectives, a conceptual formulation of an instrumentation system must be conducted. Next a feasibility study is made to determine whether the concept considered is practical and can be easily implemented. The system is then designed and benchmarked in a realistic situation.

The present investigation, as with Heath et al., [14] uses infrared thermography to monitor surface model temperatures with an applied heat flux due to a laser heating source. However, while Heath induces a heat flux along a two dimensional line, this study induces a heat flux at a discrete point and attempts to calculate an absolute heat transfer coefficient.

The concept uses an argon-ion laser to induce a discrete heat flux at a model surface in a wind tunnel. A commercially available infrared camera system measures the surface temperature at the location where the flux is applied. With a known applied heat flux and model surface temperature, the local convective heat transfer coefficient is calculated. The measurement system is mounted on a three axis positioning table which allows efficient mapping of the local convective heat transfer coefficient over an entire model surface. The optical/infrared sensing nature of this measurement system satisfies the non-intrusive requirement.

The experiment chosen to assess the performance of this technique, called the Laser-Induced Heat Flux (LIHF) technique, involves supersonic flow over a flat plate in which boundary layer transition from laminar to turbulent flow occurred. The test was conducted in the NASA Lewis Research Center 1 x 1 foot supersonic wind tunnel (SWT). Four test conditions were chosen at nominal Mach numbers of 2.5, 3.0, 3.5, and 4.0. The actual Mach numbers and test conditions are summarized in Table 1.

## Chapter 2 Experimental Apparatus and Technique

### 2.1. Laser-Induced Heat Flux Apparatus

The Laser-Induced Heat Flux (LIHF) technique determines a local convective heat transfer coefficient by monitoring the temperature distribution on a model surface with an infrared camera system as it is heated by a laser beam. In order to successfully make a measurement, the applied laser power must be known, along with the size and temperature distribution of the heated area. The infrared camera system monitors both the surface temperature and heated area size, while a sub-system must be developed to monitor and control the applied laser power. The LIHF system design used in this investigation is shown in Fig. 1. The main components of the system are essentially divided into two groups: the transmitting section, which controls and applies the laser heat flux, and the receiving section, which monitors the heating at the model surface.

The transmitting section is patterned after an optical system developed by Stinebring [15] to measure skin friction in fluid flows. It consists of an argon-ion laser which supplies the required heat flux (laser power per unit area), an attenuator/beamsplitter to control the amount of laser power directed to the model surface, an electronic shutter to control the time duration of the applied power, and a laser power meter which monitors the power of the reflected beam through the beamsplitter. An overall view of the LIHF system is shown in Fig. 1, and a detailed view of the transmitting optics is shown in Fig. 2.

When the system is in operation, the argon-ion laser is tuned to 514.5 nm, the green light wavelength. It operates in a continuous mode so that a stable power source is supplied to the transmitting optics. The laser in this investigation has a maximum power output of approximately 1.7 Watts when tuned to operate at 514.5 nm. The attenuator/beamsplitter is used to control the source laser power used in the

experiment. As the name implies, this unit splits the incoming laser beam into two perpendicular beams. Essentially, the beamsplitter transmits a portion of the incident beam and reflects the rest. The attenuator, which is adjustable, varies the power level between the two beams. The transmitted beam is used for the experiment, while the reflected beam's energy is monitored by a power meter. This technique allows for a calibration of the transmitted power applied to the model surface. After exiting the attenuator/beamsplitter assembly, the transmitted beam is controlled by a high power electronic shutter assembly. Its function is to control the time duration of the power applied at the model test surface.

The receiving section of the LIHF system is a commercially-available infrared camera system, an Inframetrics Model 600 Imaging Radiometer. It is used to determine the temperature distribution at the portion of the model surface that is heated by the incident laser beam. The infrared camera system basically is an imaging radiometer that does not measure temperature directly. A single infrared radiation detector scans the camera viewing area by the use of high-speed electromechanical galvanometers. Based on these radiation levels, the system is able to calculate a temperature based on a calibration stored in a microprocessor. However, this calibration incorporates certain assumptions about the environment where the camera system is located, so the resulting calculated temperatures are incorrect when the system is used in a non-standard situation. The system used in this investigation monitors radiation emitted in the 8–14  $\mu\text{m}$  wavelengths. A detailed description of the system used in this investigation can be found in Ref. [16]. Since the area heated by the laser beam was small, typically on the order of 10 mm, a zoom feature on the camera system allowed detailed observation of the heated area on the model.

The infrared camera system incorporates data scan conversion circuitry to convert the acquired infrared thermal images into a TV compatible output signal. This allows the data to be viewed as it is acquired on a television monitor and simultaneously be recorded by a video cassette recorder (VCR) in a standard format. Detailed data reduction is performed off-line with a PC based data reduction system using these

video tapes. The infrared camera system manufacturer developed the data reduction system.

The LIHF system installed in the NASA Lewis 1x1 SWT is shown in Fig. 1. The laser is mounted below the wind tunnel test section on a remotely-controlled three axis positioning system. Mirrors are used to direct the laser beam to the transmitting optics which are mounted above the laser on an optical breadboard with the infrared camera. The use of the positioning system allows an efficient method of remotely moving the measurement location during an experiment.

## **2.2. Wind Tunnel Facility**

The experiment was conducted in the NASA Lewis Research Center 1x1 foot supersonic wind tunnel. A schematic of the facility is shown in Fig. 3. This wind tunnel is an open loop, continuously-operating facility that uses a laboratory wide high pressure supply air system and a sub-atmospheric exhaust system to generate the pressure ratios necessary for supersonic flow.

Referring to the schematic in Fig. 3, the supply system injects air into the plenum at an angle normal to the axis of the tunnel. This insures proper diffusion and mixing as the air enters a series of screens used for flow conditioning. Note that even though the outer shell of the plenum is cylindrical, the actual shape of the plenum is rectangular. At the exit of the plenum, a two-dimensional converging nozzle is used to transition from the plenum to the converging-diverging nozzle blocks. The flow becomes supersonic as it passes through the nozzle block and then enters the constant area test section where the experimental hardware is mounted. A discussion of the experimental hardware will be presented subsequently. After the test section, the flow enters a diffusing section and dumps into the laboratory exhaust system and is eventually exhausted into the atmosphere.

The tunnel test section dimensions are nominally 30.5 cm x 31.0 cm. The tunnel test section sidewalls are replaceable. This feature allows the use of custom-designed and instrumented sidewalls for each experiment conducted in the facility. For the

present study, optical access using a zinc sulfide window is required. A schematic of the tunnel test section sidewall used in this investigation is shown in Fig. 4.

An electronically-scanned pressure system acquires the aerodynamic pressure data in the facility. In this investigation, a pressure transducer module with a full-scale measurement range of 103.425 kPa and a quoted accuracy of  $\pm 0.15$  percent of full-scale is used to measure both the model and wind tunnel reference static pressures.

Replaceable, converging-diverging nozzle blocks of fixed geometry are used for Mach number variation. Since the dimensions are fixed at the nozzle exit, the throat geometry of the blocks differ in order to produce the various Mach numbers. Currently, seven nozzle blocks are available which produce the following nominal Mach numbers: 1.3, 1.6, 2.0, 2.5, 3.0, 3.5, and 4.0. Reynolds number variation is achieved by controlling the tunnel inlet pressure. The maximum inlet pressure delivered by the laboratory supply air system is 345 kPa. The facility typically operates within a unit Reynolds number range of  $3.3 \times 10^6/\text{m}$  to  $24.0 \times 10^6/\text{m}$ .

For the present study, experiments were conducted at nominal Mach numbers of 2.5, 3.0, 3.5, and 4.0. The test conditions are summarized in Table 1. A more detailed discussion of the facility and its flow quality can be found in Ref. [17].

### **2.3. Wind Tunnel Model**

Since the objective of this investigation was to develop the LIHF system to measure the convective heat transfer coefficient in high speed compressible flows, a fundamental experiment was formulated to assess the performance of the LIHF system. The experiment chosen was supersonic flow over a flat plate, in which the boundary layer transitioned from laminar to turbulent flow. This experiment was conducted in the NASA Lewis 1x1 foot SWT. A flat plate that traversed the entire test section height was designed for the experiment. The plate was mounted at the spanwise centerline of the test section. Care was taken to mount the plate at a zero degree angle of attack relative to the tunnel freestream flow so no shock wave would

be generated in the test area. The model installed in the wind tunnel is shown in Fig. 5. This is a perspective view looking down the tunnel.

A schematic of the flat plate model is shown in Fig. 6. The nominal dimensions of the plate are 30.48 cm wide and 40.64 cm long, with a thickness of 1.27 cm. The leading edge of the plate is cut back from the front towards the rear face at a 25 degree angle. This is necessary to prevent the generation of a bow shock or a substantial oblique shock at the plate leading edge which would adversely influence the boundary layer development on the flow surface.

At an axial distance of 5.08 cm from the leading edge and symmetric about the model centerline, a 12.70 cm x 17.78 cm section of the aluminum plate was milled out to install a proofboard insert. The proofboard material is used to insulate the model heat transfer measurement area from the plate aluminum material. This technique minimizes transient heat transfer conduction effects and allows the test surface to cool to the adiabatic wall temperature almost instantaneously. Peake et al. [18] used a similar method in an experiment conducted to detect boundary layer transition with infrared thermography in a Mach 3.85 flowfield. The plate is then coated with a nominally 1 mm thick fiberglass gel-coat resin to insure uniformity of the flow surface. This coating is painted flat black to enhance its emissivity for the infrared camera measurements.

The flat plate was instrumented with six 0.51 mm diameter static pressure taps to monitor the wind tunnel conditions in the vicinity of the experimental measurement area. Taps 1, 5, and 6 were placed along the model centerline, but due to the proofboard insert, taps 2, 3, and 4 had to be located 7.62 cm below the model centerline. Two copper-constantan thermocouples were mounted on the model. The first thermocouple was placed in the aluminum material just beneath the proofboard insert. The second thermocouple was mounted on the proofboard material. It was used to monitor the flow surface adiabatic wall temperature and to calibrate the infrared camera system. This thermocouple protruded into the flow which disturbed the flat plate boundary layer. Therefore, most measurements were made upstream

of this axial location. The locations of the static pressure taps and surface-mounted thermocouple are tabulated in Table 2.

A CLEARTRAN<sup>1</sup> grade zinc sulfide window was installed in the wind tunnel sidewall assembly in order to provide optical access to the flat plate model. This material was chosen because of its ability to transmit both the green light (514.5 nm) and most of the longwave infrared (8–14  $\mu\text{m}$ ) wavelengths. An energy transmission curve of this material [19] is shown in Fig. 7. The window assembly allowed a 12.07 cm circular viewing area of the model surface.

## 2.4. Experimental Technique

The discussion of the experimental technique used in this investigation is divided into two parts. The first section discusses the LIHF system pre-test run calibration of the transmitting and receiving optics. The second section considers the data acquisition process during a typical test run, i.e., the experimental method.

### 2.4.1 LIHF System Calibration

The LIHF system components had to be calibrated before each wind tunnel test run. First, the net laser power available to heat the model test surface was determined. This step was necessary because of the transmission losses as the beam passed through the zinc sulfide window and due to the manner in which the laser power was monitored in the system setup. As discussed earlier, the LIHF system configuration shown in Fig. 2 used a power meter to monitor the reflected laser beam from the attenuator/beamsplitter assembly while the transmitted beam was used for the experiment. This reflected power level was calibrated versus the actual applied power level at the model test surface. The calibration procedure was performed as follows.

The argon-ion laser was powered up and allowed to stabilize to a predetermined power level, typically about 1.5 Watts. The high power level was required because of the transmission losses through the zinc sulfide material. When the laser stabilized,

---

<sup>1</sup> CLEARTRAN is a trademark name of a special grade of zinc sulfide available from Morton Thiokol CVD, Inc.

the calibration procedure began. An additional power meter was placed in the wind tunnel test section to monitor the transmitted laser beam power level. The attenuator portion of the attenuator/beamsplitter assembly was used to reduce the transmitted beam power level to a negligible amount in the test section. This near-zero transmitted power was recorded along with the reflected beam power level. Next, the transmitted beam power level was increased in approximately 25 mW increments until the full transmitted power level was reached, about 300 mW. At each point the transmitted and reflected power level was recorded. A first order least squares curvefit of the transmitted power,  $P_t$ , versus the reflected power,  $P_r$ , yielded the calibration coefficients used to determine the laser power level applied at the model surface during a test run. A typical calibration curve used in the investigation is shown in Fig. 8. The calibration was valid as long as the source power from the laser remained stable. Therefore, this calibration procedure was performed usually once at the beginning of each day of testing.

The next LIHF system component to be calibrated was the infrared camera system. Before taking any quantitative measurements, the infrared camera system background temperature had to be set. The background temperature consisted of the temperatures that the infrared camera detected due to the radiation of objects in its viewing area exclusive of the test article being monitored. In this investigation, the background temperature was determined by using the infrared camera to compute an average radiation level of the objects in its viewing area with the transmitted (test) laser beam attenuated. This radiation level was used by the infrared camera system's microprocessor software so that subsequent temperature measurements were not biased by the background radiation.

The infrared camera system's raw radiation level output had to be calibrated versus a known reference temperature in the wind tunnel while operating at the actual test conditions. Although the infrared camera system had the provision to calculate temperatures directly, raw radiation levels were recorded, and the rationale to do so will be discussed subsequently. This calibration was performed for each

test condition. A set tunnel freestream nominal Mach number and unit Reynolds number constituted a test condition. The conditions used in this investigation are summarized in Table 1.

For the calibration, the wind tunnel was brought on-line and allowed to stabilize at a set test condition. The LIHF system was moved by the three-axis positioning system to the surface-mounted thermocouple location on the flat plate. With the system at the proper location, the infrared camera lens zoomed in to view the thermocouple area. The laser was used as a power source to heat the thermocouple. The laser heating began at a low level and gradually was increased to the maximum power output. During this heating process, the thermocouple temperature was recorded along with the raw radiation power level output of the infrared camera system. These raw radiation level units were curvefit versus the indicated temperature which yielded a calibration curve to be used in the test data analysis.

#### **2.4.2 Experimental Method**

The experiment chosen to assess the performance of the LIHF system was to measure the convective heat transfer coefficient on a flat plate in high speed, compressible flow in which transition from a laminar to turbulent boundary layer occurred. The approach taken in this investigation was to determine the convective heat transfer coefficient at discrete points in a streamwise (axial) survey near the flat plate centerline. All measurements were made on the proofboard surface since it was insulated to minimize transverse heat conduction effects. After calibrating the LIHF system, the wind tunnel was brought on-line and set to a particular test condition.

The Mach number was set by choosing one of the removable facility nozzle blocks. The infrared camera system was used to determine the operating unit Reynolds number since Peake et al. [18] previously demonstrated that an infrared camera could be used to detect boundary layer transition in a high speed, compressible flow. The infrared camera system monitored the flat plate surface temperature distribution over

the entire proofboard surface, and the wind tunnel plenum pressure was adjusted until the transition region could be seen on the test surface.

When beginning an actual survey, the LIHF system was moved to the farthest downstream axial location on the survey line. The infrared camera lens zoomed in to focus on as small a viewing area as possible since the heated area on the plate was on the order of 10 mm. The test laser power was adjusted to a constant level with the attenuator/beamsplitter assembly while the shutter in the transmitting optics was closed in order to prevent surface heating. The test laser power remained constant during the entire survey. When the survey began, the shutter was opened and the laser beam heated the test surface spot for approximately 10 seconds. During this time, the infrared camera system recorded the entire heating process on a video tape for future data reduction. At the end of the heating interval, the shutter was closed to prevent further surface heating, and the LIHF system moved 5 mm to the next upstream axial location in the survey line. This process was repeated until the completion of the axial survey.

## Chapter 3 Analysis

### 3.1. Data Reduction

The experimental test Mach numbers and unit Reynolds numbers were determined from thermodynamic and isentropic flow relationships listed in Ref. [20]. These relations are discussed in Appendix A of this investigation. The measured plenum total pressure and temperature were used to calculate Mach number and unit Reynolds numbers. The number three static pressure tap on the model was used to determine the wind tunnel freestream conditions in the vicinity of the flat plate, while all static pressure taps on the flat plate were used to determine the local Mach number distribution external to the flat plate boundary layer.

The heat transfer raw data reduction consists of interpreting the thermal images acquired by the infrared camera system. As discussed earlier, the infrared camera portion of the LIHF system monitors the model surface radiation emission as it is heated locally by the laser beam. The spot temperature distribution must be determined along with the size of the heated area. A typical infrared camera thermogram of the flow surface area affected by the laser heating is shown in Fig. 9.

The infrared camera system has the provision to calculate temperatures directly from the observed radiation emission by using its own microprocessor-based software. However, this option was not used because private communication with the infrared camera system's manufacturers indicated that the software was not adequate for temperature measurements in a wind tunnel application. This is due mainly because of the severe static pressure gradient in the measurement environment. The infrared camera medium is at atmospheric pressure, while the test model is at a significantly lower static pressure, typically about 0.01 atmosphere. Therefore, for each test condition in this study, a calibration curve of radiation level versus temperature was

used to determine the test model local temperature. The calibration approach was discussed in Section 2.4.1 of this investigation.

Considering the thermogram shown in Fig. 9, it is necessary to determine the extent of the heated area. That is, the temperature distribution as a function of the spot radius is needed to properly assess the model heat transfer characteristics. The data reduction package supplied by the manufacturer has provisions to determine the radial distance for a specific temperature. Use of this feature allows one to determine the heated area temperature distribution as a function of the spot radius at each survey point.

### **3.2. Heat Transfer Analysis**

In order to determine the heat transfer characteristics of the flat plate in supersonic flow, one must understand the physical processes that are occurring with both the measurement technique and the aerodynamic heat transfer. A knowledge of the physical processes involved allows one to construct an analytical model to determine the local convective heat transfer coefficient. In this case, the laser beam induces a local flux that heats the model surface. The heating causes radial heat conduction in the model fiberglass gel-coat resin which was used to give the flat plate a uniform surface finish. In addition to the heat conduction, convective heat transfer due to the fluid flow tends to cool the heated area.

In this study, it was observed that as soon as the heat flux was applied, the local heated region would grow very rapidly, but after approximately 10 seconds, the heated area would come to an equilibrium state in which the spot size would remain constant with little surface temperature change. During the transient time period, the heated area diameter grows from the initial laser beam diameter of 1.3 mm to a steady-state diameter about 10 times as large. The rapid radial heat conduction tends to balance the excess heat flux. Convective heat transfer occurs during the entire process and also helps to balance the excess heat flux. An equilibrium or steady-state condition is reached when both the heat conduction and convection balances the excess heat flux.

The analysis used to determine the local convective heat transfer coefficient is performed at the steady-state condition, i.e., when the excess applied heat flux is balanced by the radial heat conduction and convection. The analytical method used in this study is similar to one used by Schneider [21] for heat transfer with convection in a nonadiabatic plate with a local heat source. In the present study, the gel-coat fiberglass resin coating on the insulated portion of the flat plate is the test surface where the heat flux (source) is applied. Therefore, one side of the material is insulated, and convection occurs only at the flow surface. Figure 10 shows a schematic of the test surface used for the analysis.

Referring to Fig. 10, a source of strength  $q_0$  and radius  $r_s$  heats the gel-coat resin of thickness  $\delta$ . Before the heat flux is applied, the test surface temperature is at the adiabatic wall temperature. Convection occurs at the flow surface while the lower surface is insulated. An energy balance at a radial distance  $r$  from the center of the source at the steady state condition yields the following

$$q_r = q_{r+dr} + q, \quad (3.2-1)$$

where

$$q_r = -kA_r \frac{\partial T_r}{\partial r} = -2\pi r \delta k \frac{\partial T}{\partial r}, \quad (3.2-2)$$

and

$$q_{r+dr} = q_r + \frac{\partial(q_r)}{\partial r} = -2\pi r \delta k \frac{\partial T}{\partial r} - 2\pi \delta k \left[ \frac{\partial(rT)}{\partial r} \right] dr. \quad (3.2-3)$$

Simplifying this expression ,

$$q_{r+dr} = -2\pi r \delta k \left( \frac{\partial^2 T}{\partial r^2} dr + \frac{1}{r} \frac{\partial T}{\partial r} dr + \frac{\partial T}{\partial r} \right). \quad (3.2-4)$$

Now, the convective portion of the energy balance becomes,

$$q = 2\pi r h (T - T_{aw}) dr. \quad (3.2-5)$$

Combining these terms yields the following partial differential equation that describes the heat transfer process due to the applied heat flux on the flat plate model surface,

$$\frac{\partial^2 T}{\partial r^2} + \frac{1}{r} \frac{\partial T}{\partial r} - \frac{h}{k\delta} (T - T_{aw}) = 0. \quad (3.2-6)$$

Now, defining a new variable,  $\theta = T - T_{aw}$ , the equation can be rewritten as follows,

$$r^2 \frac{\partial^2 \theta}{\partial r^2} + r \frac{\partial \theta}{\partial r} - r^2 \frac{h}{k\delta} \theta = 0, \quad (3.2-7)$$

which is recognized as a modified Bessel's equation with the following solution,

$$\theta = C_1 I_0 \left( \sqrt{\frac{h}{k\delta}} r \right) + C_2 K_0 \left( \sqrt{\frac{h}{k\delta}} r \right). \quad (3.2-8)$$

$I_0$  is a modified Bessel function of the first kind, of order 0, and  $K_0$  is a modified Bessel function of the second kind, of order 0. The requirement that the solution to remain finite as  $r \rightarrow \infty$  requires that  $C_1 = 0$  so,

$$\theta = C_2 K_0 \left( \sqrt{\frac{h}{k\delta}} r \right). \quad (3.2-9)$$

Applying the steady state heat conduction relationship at the location of the applied heat flux,

$$q_o = -k A_{r_s} \left( \frac{\partial T}{\partial r} \right)_{r=r_s}, \quad (3.2-10)$$

we solve for the constant,  $C_2$ . The resulting analytical temperature solution becomes

$$T(r) = T_{aw} + \frac{q_o}{2\pi\sqrt{hk\delta}r_s} \frac{K_0 \left( \sqrt{\frac{h}{k\delta}} r \right)}{K_1 \left( \sqrt{\frac{h}{k\delta}} r_s \right)}, \quad (3.2-11)$$

where  $k$  is the thermal conductivity of the material,  $h$  is the convective heat transfer coefficient, and  $K_0$  and  $K_1$  are modified Bessel functions of the second kind of order 0 and 1, respectively.

Equation 3.2-11 yields an expression for the local steady-state temperature distribution on the flat plate due to the applied heat flux from the laser beam. All quantities are known except for the convective heat transfer coefficient,  $h$ . The experimental spot temperature distribution,  $T(r)$ , is known from the infrared camera system measurements. Therefore, the heat transfer coefficient term in the equation can be varied until the analytical solution matches the experimental data. Using this approach, the local heat transfer coefficient for a discrete point on the flat plate is determined.

## Chapter 4 Results and Discussion

### 4.1. Flow Surface Thermal Images

As a means of assessing supersonic flow development on a flat plate as it transitioned from laminar to turbulent flow, Peake et al. [18] demonstrated that infrared thermography could be used to determine the extent of a flat plate transition region in supersonic flow. In the present investigation, the infrared camera portion of the LIHF system was used for this purpose. That is, for each test condition where heat transfer measurements were made, the infrared camera monitored the overall surface temperature distribution on the insulated portion of the flow surface.

Since this investigation was conducted in a supersonic wind tunnel, the tunnel total pressure control valve was used to vary the unit Reynolds number which moved the transition region on the flat plate. The ability to monitor the flat plate surface temperature distribution with the infrared camera system allowed the laminar to turbulent transition location on the flat plate to be precisely controlled.

A typical surface infrared thermogram of the flat plate is shown in Fig. 11. In this photo, the circular outline of the zinc sulfide window can be seen as it allows transmission of the infrared radiation from the flat plate flow surface. Within the viewing area, the qualitative flat plate surface temperature distribution can be seen. In this case the tunnel nominal Mach number is 4.0, and the flow proceeds from left to right. The edges of the insulated portion of the flow surface clearly can be seen as the sharp temperature gradients at the lower and right side of the viewing area. This gradient occurs because the heat conduction in the aluminum material has not allowed this area of the flow surface to cool to the adiabatic wall temperature.

Three distinct regions on the insulated surface can be observed, but since this photo was converted from a color to gray scale format, a detailed explanation of the surface temperature distribution is needed because this conversion leaves some

ambiguity in the interpretation of the temperatures. Notice that the gray scale at the very bottom of the photo shows eight different temperature regions which indicate colder to hotter temperatures from left to right.

The first region is the laminar flow region and is located at the left side of the image. It is characterized by a rather uniform temperature distribution except for the anomaly in the upper left portion of the region that shows a spot of cooler temperature. This anomaly is actually a window reflection that superimposes the infrared camera lens on the thermal image.

As the flow proceeds downstream it begins to transition to turbulent flow. This is seen by the second region in the photograph. It is characterized by a jagged axial temperature gradient region which spans the flat plate. Here, the flat plate surface temperature increases to a maximum at the center of this transition region and then begins to decrease.

Near the top of this transition region, the temperature distribution indicates a spot where the temperature appears to be hottest. This is the location of the surface-mounted thermocouple which is used for temperature calibration purposes. Some local heating may be expected since the thermocouple protrudes into the flow and probably induces a local weak shock wave at this location. However, the thermocouple is mounted to the surface with an epoxy material whose emissivity does not match that of the plate surface. This mismatch yields incorrect temperature readings in this area.

Immediately downstream of the transition, a turbulent flow region can be seen which is again characterized by a relatively uniform temperature distribution. Here, the temperatures are lower than observed in the transition region. This indicates that the turbulent adiabatic wall temperature is lower relative to what is seen in the transition region. Since this region is at the very rear edge of the insulated portion of the flow surface, its viewing area is limited. In fact, at two spanwise locations, the transition region extends to the rear edge of the insulated surface.

This infrared thermogram image is showing the variation in the adiabatic wall

temperature as the flow transitions from laminar to turbulent. The change in adiabatic wall temperature can be related to the change in wall temperature recovery factor by equation A-3 in Appendix A. The generally accepted recovery factor for laminar flow is taken to be the square root of the Prandtl number while the turbulent recovery factor is the cube root of the Prandtl number [22]. For air, the Prandtl number is 0.72, and the laminar and turbulent recovery factors become 0.85 and 0.89, respectively. However, in the transition region, the recovery factor varies significantly as evidenced by the change in the adiabatic wall temperatures shown in Fig. 11.

These same trends in the adiabatic wall temperature variation through the transition region were observed in Peake's investigation of transition on a flat plate in a Mach 3.85 flowfield [18]. In his investigation, the adiabatic recovery factor was 0.867 in the laminar region just before transition, and peaked to a value of 0.893 at the maximum adiabatic wall temperature location in the transition region. The recovery factor steadily decreased in the rear portion of the transition region to an observed turbulent value of 0.876. Peake's observed recovery values are higher in the laminar region and lower in the turbulent region when compared to the generally accepted values. He attributes this discrepancy to wind tunnel effects such as acoustic noise and freestream turbulence.

In this investigation, measurements were made at the Mach 3.0 and 3.5 conditions in an attempt to quantify the change in wall recovery in the transition region. This was done by monitoring the surface radiation emission similar to what was seen in Fig. 11. However, as mentioned in the Experimental Technique section of this study, the infrared camera system's raw radiation levels were related to temperatures by a calibration process which used laser heating to vary the observed temperature. This calibration procedure yielded a temperature calibration curve with radiation levels higher than those seen on the flat plate, so accurate temperatures could not be determined. Therefore, the variation in recovery factor could not be determined for this study. Because of this, the heat transfer measurements which will be presented subsequently uses a constant laminar recovery factor of 0.85 for all measurements.

## 4.2. Static Pressure Measurements

The flat plate model was instrumented with limited static pressure taps that were used primarily to monitor the aerodynamic conditions during a test run. However, the static pressure data may also provide some insight in interpreting the heat transfer data and are presented here for the sake of completeness. Before discussing these results, it is important to note that the pressure transducer used for these measurements was not accurate for the precise static pressure measurements needed to quantify the detailed boundary layer development on a flat plate, but was accurate enough to assess the overall model performance for major instabilities such as model unstart, flow separation, etc. Data point error bars are included to indicate measurement uncertainties. A discussion of these uncertainties can be found in Appendix B.

Figures 12 to 15 show the results of surface static pressure measurements that were made simultaneously with the heat transfer measurements. In these figures, the open symbols represent static pressure taps located on the model axial centerline, while the closed symbols are static pressure taps 7.62 cm below the model centerline. As mentioned in the Wind Tunnel Model section of this investigation, this offset of the axial static pressure taps is necessary due to the placement of the insulated proofboard insert on the flow surface. For these and all subsequent results, the coordinate system origin is taken to be on the model centerline at the flat plate leading edge. Refer to Fig. 6 for the definition of the coordinate system.

Examination of the static pressure distributions show that the surface static pressures are relatively well-behaved when the measurement uncertainties are taken into consideration. In each plot, the static pressures are nondimensionalized by the number one static pressure tap which is located at approximately 10 percent of the plate length on the model centerline. No indication of model unstart or flow separation on the model surface was detected for any of the test conditions.

For the Mach 2.5 results shown in Fig. 12, there is a slight static pressure rise at static tap number five which is located on the model centerline at approximately 62

percent of model length. This is indicative of a weak shock or Mach line emanating from the flat plate just upstream of this location. This disturbance probably originates at the surface-mounted thermocouple and propagates outward to this location on the model centerline. Most heat transfer measurements are made upstream of the surface-mounted thermocouple in the undisturbed region of the flat plate boundary layer.

The Mach 3.0, 3.5, and 4.0 surface static pressure distributions shown in Figs. 13, 14, and 15, respectively are smoother than the Mach 2.5 results, but there are indications of Mach lines impinging on the flat plate boundary layer. These are characterized by the slight step changes in the static pressure distributions. For the Mach 3.0 case, the number 3 static pressure tap is affected, while the affected regions move progressively upstream for the Mach 3.5 and 4.0 cases. These disturbances probably are caused by the slight mismatch between the wind tunnel nozzle blocks and the test section. Note that the nozzle blocks are replaced in order to change the wind tunnel freestream Mach number, and the potential for a slight mismatch at the tunnel nozzle block/test section interface exists.

If the disturbances impinging on the flat plate boundary layer are of sufficient strength, they will prematurely force the laminar boundary layer to transition to turbulent flow. It is felt that these disturbances were Mach lines and were not strong enough to cause premature boundary layer transition. The overall flow surface thermal images monitored at these conditions showed no evidence of premature boundary layer transition.

### **4.3. Local Mach Number Distributions**

With the local static pressure distributions on the flat plate known, the local Mach number distribution external to the flat plate boundary layer can be determined. Equation A-1 from Appendix A relates the local static pressure and total pressure to a local Mach number providing the following assumptions are made: (1) the measured local wall static pressure is equivalent to the local freestream static pressure since there is a negligible static pressure gradient in the boundary layer normal to the flat

plate, and (2) the wind tunnel total pressure is equivalent to the local total pressure at the static pressure measurement locations.

Schlichting [23], in an analysis of flat plate boundary layers demonstrates that condition (1) is a valid assumption. However, condition (2) is valid only if there are no strong shock waves in the flow that would cause total pressure losses. The static pressure results presented earlier indicate the presence of some disturbances in the form of weak shocks or Mach lines. It is felt that the total pressure losses due to these disturbances are minimal, and the use of the wind tunnel total pressure alone would not grossly misrepresent the external Mach number distributions of the flat plate boundary layer. Therefore, the Mach number distributions external to the flat plate boundary layer which will be presented subsequently are calculated by using the static pressure distributions shown in Figs. 12 thru 15 and the corresponding wind tunnel total pressures.

The local Mach number distributions at the edge of the flat plate boundary layer are shown in Figs. 16 to 19. As before, error bars are included to show the uncertainties in the Mach number calculation. The Mach number uncertainties are estimated by using the limits of the static pressure measurement errors presented earlier. As seen in the static pressure results, the Mach number distributions are well behaved considering the measurement uncertainties. The distributions are smoothest at the higher freestream nominal Mach number conditions.

These results also show the same trends as observed in the surface static pressure distributions. For the nominal freestream Mach number of 2.5, the effects of the surface-mounted thermocouple are seen. The disturbance that emanates from the thermocouple causes a Mach number loss consistent with the static pressure rise seen at the same location. Similar trends at the higher Mach numbers are also apparent. That is, at the same locations where the surface static pressures rise due to impinging Mach lines, corresponding Mach number losses are seen.

## 4.4. Heat Transfer Measurements

As stated earlier, the main objective of this investigation is to develop a non-intrusive technique to measure local convective heat transfer coefficients in high speed flows. The design and implementation of the LIHF system was discussed previously. Now, the results of the application of the technique to a practical flow situation, supersonic flow over a flat plate, will be presented. This discussion will be divided into two parts. Part one presents the results of the LIHF system temperature calibration which was discussed in the Experimental Technique section of this study. In Part two of this section, the actual heat transfer measurements are presented.

### 4.4.1 LIHF System Temperature Calibration

In order to determine the local convective heat transfer coefficient at a point on the model surface, a calibration had to be performed to relate the raw radiation levels sensed by the infrared camera to actual surface temperatures. This calibration procedure was discussed earlier, and these results are now presented.

The temperature calibration data used in this study are shown in Fig. 20. For each case, the data were approximated by a second order least squares polynomial curvefit. The curvefit results were used to determine the local temperature distributions. In the case of the Mach 3.5 results, two calibration runs were performed, and a separate curvefit was performed for each of the runs. When the Mach 3.5 infrared camera measurements were analyzed, both curvefits were used and the results were averaged to determine the local model surface temperature distributions.

When examining the curvefit results, most of the data show similar trends, except for the Mach 3.0 calibration data which did not follow the other data. Table 1, which lists the wind tunnel facility conditions for each calibration run indicates that this anomaly is independent of the facility total temperature and static pressure. There may be a Reynolds number dependence as the Mach 3.0 case was conducted at the lowest Reynolds number in this study. However, examination of the Mach 2.5, 3.5,

and 4.0 data do not support the Reynolds number variation hypothesis. These data show no strong Reynolds number dependence.

Another explanation for the Mach 3.0 data anomaly could be the result of a variation in atmospheric conditions external to the wind tunnel. This study was conducted over a three day interval. On day one of the investigation, the Mach 3.0 tests were performed. The Mach 2.5 and 4.0 data were gathered on day two, while the Mach 3.5 test was conducted on day three. It is quite possible that some factor external to the wind tunnel environment influenced the infrared camera system's radiation measurements.

#### **4.4.2 Experimental Convective Heat Transfer Coefficients and Comparison with Theory**

The results presented here are the experimental heat transfer measurements for supersonic flow over a flat plate. The local convective heat transfer coefficients are obtained by using both the LIHF technique and analysis discussed in this investigation. Comparison of the data are made to laminar flow boundary layer theory developed by Van Driest [24] as presented by Kays [22].

The theory solves the momentum and energy equation for a high speed laminar boundary layer with variable properties. A Prandtl number of 0.75 is assumed, and a solution in the form of  $St\sqrt{Re_x} = f\left(M, \frac{T_w}{T}\right)$  is obtained. This graphical solution is shown in Fig. 21. With the Mach number external to the flat plate and the wall temperature ratio known, the theoretical local convective heat transfer coefficient can be found. This procedure was applied and these results are presented with the experimental data.

In the analysis of the experimental data, a constant laminar recovery factor of 0.85 was used to calculate the flat plate adiabatic wall temperature throughout the entire flowfield. This assumes a Prandtl number of 0.72. The theoretical analysis, however, assumes a Prandtl number of 0.75, so a slight mismatch may occur when comparing the experimental results to the theoretical analysis.

Also, as noted earlier, a portion of the flow is transitional, so both the theory and experimental results are not strictly correct in this region. The theoretical analysis assumes laminar flow only and does not consider transition. The derived experimental convective heat transfer coefficients do not take into account the variation of wall recovery factor in the transition region. As mentioned earlier, an unsuccessful attempt was made to determine the variation in wall recovery factor in the boundary layer transition region.

The experimentally-determined convective heat transfer coefficients and comparison with the theory are shown in Figs. 22–25. In general, the experimental heat transfer coefficients are higher than theoretical predictions. Some of this discrepancy could be attributed to the data reduction approach which depends on a precise knowledge of the gel-coat thermal conductivity. Unfortunately, the manufacturer of the gel-coat resin used in this investigation (REN 1129 by Ciba-Geigy) has never determined the thermal conductivity of this material. Therefore, a value of the thermal conductivity was assumed based on published values of similar materials.

For all test cases, the flat plate boundary layer begins to transition in the measurement region, and transition proceeds to the end of the measurement region without the flow becoming fully turbulent. The approximate locations of the onset of transition were determined and are shown in Figs. 23 and 24 for the Mach 3.0 and 3.5 cases, respectively. Unfortunately, for the Mach 2.5 and 4.0 conditions, Figs. 22 and 25, the location of the onset of transition was not determined.

At the Mach 2.5 condition, the experimentally-determined heat transfer coefficients shown in Fig. 22 generally follow the trend of the laminar flow theory, but the experimental values are higher than predicted, and there are some scatter in the data. Some of the data scatter are attributed to measurement uncertainties which are discussed in Appendix C. There could be some instabilities in the flow at this condition, because the static pressure results presented earlier for the Mach 2.5 case also showed significant data scatter.

For the Mach 3.0 results shown in Fig. 23, there are less scatter in the experimental data. At the beginning of the measurement region, the experimental results show heat transfer coefficients lower than what the theory predicts that gradually recover to overshoot the theoretical predictions. It appears that this is a gradient region in which the flow is adjusting to some disturbance. The static pressure measurements for this condition presented in Fig. 13 do show the presence of an adverse pressure gradient region where these measurements were made.

From an axial location of 27 percent to 33 percent of model length, a region exists where the experimental convective heat transfer coefficients appear to have reached a plateau and are relatively constant when compared to the trend in the theoretical values. Next, comes the onset of transition in which the experimental convective heat transfer coefficients take a step change downward towards the theoretical predictions. The corresponding static pressure distribution also shows a step change at this location to begin a favorable pressure gradient run which extends to the end of the heat transfer measurement region. It is interesting to note that in this transition region, the derived experimental convective heat transfer coefficients tend to follow the theoretical laminar flow trends.

The Mach 3.5 heat transfer results presented in Fig. 24 show significant data scatter upstream of the transition location. The data scatter in this region are attributed to problems in the data acquisition process at this condition. During the data reduction process, it was observed that the time duration of the applied heat flux was not long enough to allow the heated region to stabilize to a steady state local surface temperature distribution. The analysis used to determine the convective heat transfer coefficient based on the surface temperature distribution is a steady state analysis so the experimental results upstream of the transition location are questionable.

In the transition region, the Mach 3.5 experimentally-determined convective heat transfer coefficient distribution becomes well behaved and settles out to values higher than is expected for a laminar boundary layer. Again, the experimental results assume a constant recovery factor in this region. In reality, the recovery factor does vary

in the transition region, so the experimentally-determined convective heat transfer coefficients presented here are not accurate.

The Mach 4.0 results are shown in Fig. 25. At this condition two separate surveys were conducted at different applied laser heat flux power levels. Both results indicate higher heat transfer than the theoretical laminar flow predictions, and there is more data scatter for the higher applied heat flux power case. This data scatter could be a result of the heated areas not coming to a steady state condition in the allotted time interval during the data acquisition process.

Examination of the lower applied heat flux results at Mach 4.0 show similar behavior as the Mach 3.0 results. Up to an axial location of 22 percent of model length, there is evidence of a slight heat transfer gradient region followed by relatively constant heat transfer region. The Mach 4.0 static pressure distribution presented in Fig. 15 does show evidence of an adverse pressure gradient at this location on the model. Next comes a region of rapidly decreasing heat transfer followed by a region of convective heat transfer characterized by a slight gradient. This region begins at an axial location 32 percent of model length and proceeds to the end of the measurement region. Although the location of the onset of transition was not determined for this condition, the data trends here are very similar to those seen in the Mach 3.0 and 3.5 transition regions.

If one considers the fact that these heat transfer measurements were made to demonstrate the feasibility of a new measurement technique, the results presented here are reasonable. In Ref. [5] Kaufman II and Johnson present convective heat transfer measurements for undisturbed laminar boundary layers at Mach 8 and unit Reynolds numbers of 2 to 6 million per meter. They measured convective heat transfer coefficients in the range of 2.0 to 8.5 W/m<sup>2</sup>K over the range of Reynolds numbers in the study. The present investigation was conducted at similar Reynolds numbers, but at lower Mach numbers. The experimental convective heat transfer coefficients presented in this investigation are in the same range measured by Kaufman II and Johnson.

Gulbran et al. [6] presented convective heat transfer measurements for an undisturbed laminar boundary layer at Mach numbers of 6, 8, and 10 at a unit Reynolds number of 3.2 million per meter. They measured convective heat transfer coefficients of 1.2 to 3.0 W/m<sup>2</sup>K which are slightly lower than the values seen in the present study. This is expected since the experiments of Gulbran et al. were conducted at higher Mach numbers and a lower Reynolds number. The measured convective heat transfer coefficient distributions presented by Gulbran et al. for the undisturbed laminar boundary layers do show data scatter similar to what was seen in the present study. In their experiments, the worst data scatter was seen at the Mach 6.0 condition where a 50 percent difference in convective heat transfer coefficients was observed at adjacent measurement locations. This is an indication that precise measurements of convective heat transfer in an undisturbed laminar boundary layer are difficult to make.

## Chapter 5 Concluding Remarks

An investigation has been conducted to develop an instrumentation system capable of high resolution surface heat transfer measurements in complex, three-dimensional high speed flows. The concept conceived in this study to make these heat transfer measurements is a laser-induced heat flux technique (LIHF) which uses a laser to induce a local heat flux at a point on a model surface. During the application of the heat flux, an infrared camera system monitors the surface temperature distribution, and a local convective heat transfer coefficient is determined by an analysis of the area affected by the local heating.

In order to assess the feasibility of this concept, the LIHF technique was used to make surface convective heat transfer measurements for flat plate transitional boundary layers in high speed flows. The experiments were conducted over a nominal Mach number range of 2.5 to 4.0. These measurements were presented and compared to theoretical convective heat transfer coefficient distributions for high speed laminar boundary layers. The results compared reasonably well with theory, but some scatter in the experimental data was observed. Some of the data scatter was attributed to minor problems in the data acquisition process. Also, because of the approach used for the temperature calibration of the infrared camera system, the variation in adiabatic wall temperature recovery factor could not be determined, and the resulting convective heat transfer coefficients determined for the transitional portion of the flat plate boundary layers were not accurate.

Overall, the results of this investigation indicate that the LIHF concept is a viable surface convective heat transfer measurement technique. Future studies will use the LIHF technique to make heat transfer measurements in complex, three-dimensional high speed flows, specifically shock wave/turbulent boundary layer interaction studies. However, in order to make quality high resolution convective

heat transfer measurements, an improved temperature calibration approach must be developed for the infrared camera system so that local changes in the model adiabatic wall temperatures can be resolved.

## Bibliography

- [1] Gardon, R., "A Transducer for the Measurement of Heat-Flow Rate," *Trans. ASME, Journal of Heat Transfer*, vol. 82, pp. 396-398, November 1960.
- [2] Hayashi, M., Sakurai, A., and Aso, S., "Measurement of Heat-Transfer Coefficients in Shock Wave-Turbulent Boundary Layer Interaction Regions with a Multi-Layered Thin Film Heat Transfer Gauge." NASA TM 77958, January 1986.
- [3] Holloway, P., Sterrett, J., and Creekmore, H., "An Investigation of Heat Transfer Within Regions of Separated Flow at a Mach Number of 6.0." NASA TN D-3074, November 1965.
- [4] Johnson, C. and Kaufman II, L., "Interference Heating From Interactions of Shock Waves With Turbulent Boundary Layers at Mach 6." NASA TN D-7649, September 1974.
- [5] Kaufman II, L. and Johnson, C., "Weak Incident Shock Interactions with Mach 8 Laminar Boundary Layers." NASA TN D-7835, December 1974.
- [6] Gulbran, C., Redeker, E., Miller, D., and Strack, S., "Heating in Regions of Interfering Flow Fields, Part III: Two-Dimensional Interaction Caused by Plane Shocks Impinging on Flat Plate Boundary Layers." AFFDL-TR-65-49, March 1967.
- [7] Van Fossen Jr., G., "Heat Transfer Coefficients for Staggered Arrays of Short Pin Fins." NASA TM 81596, March 1981.
- [8] Vogel, J. and Eaton, J., "Heat Transfer and Fluid Mechanics Measurements in the Turbulent Reattaching Flow Behind a Backward-Facing Step," Tech. Rep. MD-44, Thermosciences Div., Dept. of Mech. Eng., Stanford University, 1984.
- [9] Eibeck, P. and Eaton, J., "An Experimental Investigation of the Heat-Transfer Effects of a Longitudinal Vortex Embedded in a Turbulent Boundary Layer," Tech. Rep. MD-48, Thermosciences Div., Dept. of Mech. Eng., Stanford University, 1985.

- [10]Pauley, W. and Eaton, J., "The Fluid Dynamic and Heat Transfer Effects of Streamwise Vortices Embedded in a Turbulent Boundary Layer," Tech. Rep. MD-51, Thermosciences Div., Dept. of Mech. Eng., Stanford University, 1988.
- [11]Hippensteele, S., Russell, L., and Stepka, F., "Evaluation of a Method for Heat Transfer Measurements and Thermal Visualization Using a Composite of a Heater Element and Liquid Crystals." NASA TM 81639, March 1981.
- [12]Hippensteele, S. and Russell, L., "High-Resolution Liquid-Crystal Heat-Transfer Measurements on the End Wall of a Turbine Passage with Variations in Reynolds Number." NASA TM 100827, July 1988.
- [13]Carlomagno, G. and De Luca, L., "Heat Transfer Measurements By Means of Infrared Thermography," tech. rep., Institute of Gasdynamics, University of Naples, Naples, Italy, 1986.
- [14]Heath, D., Winfree, W., Carraway, D., and Heyman, J., "Remote Noncontacting Measurements of Heat Transfer Coefficients for Detection of Boundary Layer Transition in Wind Tunnel Tests," in *ICIASF '87*, (The College of William and Mary, Williamsburg, VA), pp. 135-139, June 22-25, 1987.
- [15]Stinebring, D., "Development of the Liquid Crystal/Skin Friction Measurement Device," in *Flow Visualization III: Proceedings of the Third International Symposium on Flow Visualization* (W.J. Yang, ed.), (University of Michigan, Ann Arbor, MI), pp. 49-54, September 6-9, 1983.
- [16]"Inframetrics Model 600 Operations Manual." Inframetrics, Inc., Billerica, MA.
- [17]Skebe, S., *Experimental Investigation of Two Dimensional Shock Boundary Layer Interactions*. PhD thesis, Case Western Reserve University, Cleveland, OH, 1983.
- [18]Peake, D., Bowker, A., Lockyear, S., and Ellis, F., "Non-Obtrusive Detection of Transition Region Using an Infra-Red Camera," in *AGARD-CP-224 Laminar-Turbulent Transition*, May 1977.
- [19]"Advanced Materials Brochure." Morton Thiokol CVD, Inc., Woburn, MA.

- [20]Ames Research Staff, "Equations, Tables, and Charts for Compressible Flow." NACA Report 1135, 1953.
- [21]Schneider, P., *Conduction Heat Transfer*. Second printing, Reading, MA: Addison-Wesley Publishing Company, Inc., September 1957.
- [22]Kays, W. and Crawford, M., *Convective Heat and Mass Transfer*. New York, NY: McGraw-Hill Book Company, 1980.
- [23]Schlichting, H., *Boundary-Layer Theory*. New York, NY: McGraw-Hill Book Company, 7th ed., 1979.
- [24]Van Driest, E., "Investigation of Laminar Boundary Layer in Compressible Fluids Using the Crocco Method." NACA TN-2597, January 1952.

## Appendix A Thermodynamic and Isentropic Relations

The Mach number is determined from the following relationship,

$$M = \sqrt{\frac{2}{\gamma - 1} \left\{ \left( \frac{P_o}{p} \right)^{\frac{\gamma - 1}{\gamma}} - 1 \right\}} \quad (\text{A-1})$$

where  $\gamma$  is the ratio of specific heats (for air,  $\gamma=1.4$ ),  $P_o$  is the plenum total pressure, and  $p$  is the local wall static pressure. Since this relation assumes that the flow is isentropic, we assume that no substantial shock emanates from the leading edge of the flat plate when using it to calculate the local Mach number external to the flat plate boundary layer. Also, the static pressure throughout the boundary layers are assumed to be constant and are equal to the measured wall value.

The static temperature is calculated from the following,

$$T = \frac{T_o}{1 + \frac{\gamma - 1}{2} M^2} \quad (\text{A-2})$$

With both the freestream total and static temperatures known, the flow surface adiabatic wall temperature can be calculated by the relationship,

$$T_{aw} = \left( 1 + r_c \frac{\gamma - 1}{2} M^2 \right) T, \quad (\text{A-3})$$

where  $r_c$  is the recovery factor.

In order to determine the Reynolds number, the flow velocity and fluid density must be calculated. The flow velocity is calculated by

$$V = Ma, \quad (\text{A-4})$$

where  $a$  is the local speed of sound and is determined from the following,

$$a = \sqrt{\gamma RT}. \quad (\text{A-5})$$

The fluid density is calculated by the ideal gas relationship,

$$\rho = \frac{p}{RT} . \quad (\text{A-6})$$

With these variables known, the Reynolds number can be found by

$$Re = \frac{\rho V l}{\mu} , \quad (\text{A-7})$$

where the viscosity,  $\mu$ , is found from Sutherland's viscosity law,

$$\mu = 1.458 \times 10^{-6} \frac{T^{\frac{3}{2}}}{T + 110.56} \left[ \frac{Ns}{m^2} \right] . \quad (\text{A-8})$$

## **Appendix B Estimation of Static Pressure and Mach Number Uncertainty**

A sample error uncertainty analysis is performed for the number one static pressure tap reading at the Mach 4.0 condition which is the worst case for this study. The indicated model surface static pressure at this condition is 1.38 kPa. The pressure transducer used to make all static pressure measurements has a rated accuracy of  $\pm 0.15$  percent of a full scale value of 103.425 kPa. This yields a maximum pressure reading uncertainty of  $\pm 0.155$  kPa. Subtracting and adding this value to the measured static pressure value of 1.38 kPa gives an error band of 1.225 to 1.535 kPa.

The Mach number uncertainties can be found by applying the limits of the static pressure uncertainty to equation A-1 of Appendix A which relates static pressure to Mach number. This yields a Mach number uncertainty range of 3.91 to 4.08, while the calculated Mach number for the indicated static pressure measurement of 1.38 kPa is 3.99.

## Appendix C Estimation of Convective Heat Transfer Coefficient Uncertainty

The determination of the convective heat transfer coefficient at each measurement point in this investigation depends on the radial temperature distribution in the heated region. Equation 3.2-11 relates the local temperature distribution to the local convective heat transfer coefficient. In determining the radial temperature distribution for each point, the PC based data reduction system had to digitize the infrared camera images that were stored on VHS format videocassettes. This process decreased the resolution of the observed temperature distribution, and a discussion of this uncertainty follows.

This discussion will consider the convective heat transfer measurement for the Mach 2.5 condition at  $x/L = 0.21$ . At this point the analysis determined a measured heat transfer coefficient of  $16.6 \text{ W/m}^2\text{K}$ . It was observed that the uncertainty in each raw infrared camera radiation measurement was  $\pm 9$  units. Therefore, for each radial measurement, this uncertainty was added and subtracted from the original baseline measurements that were used to get the heat transfer coefficient of  $16.6 \text{ W/m}^2\text{K}$ . This process yielded an upper and lower bounds for the baseline radial temperature distribution measurements. These upper and lower bounds of the baseline radial temperature distribution were then used in equation 3.2-11 to determine the measurement uncertainty. This yields an uncertainty band of  $15.2$  to  $18.4 \text{ W/m}^2\text{K}$  about the original measurement of  $16.6 \text{ W/m}^2\text{K}$  which is equivalent to a  $\pm 10$  percent measurement uncertainty.

Table 1. Experimental Conditions

| Nominal Mach Number | Actual Mach Number | Tunnel Total Pressure (kPa) | Tunnel Static Pressure (kPa) | Tunnel Total Temperature (K) | Reynolds No. ( $\times 10^{-6} \cdot m$ ) | Applied Heat Flux (mW) | Spanwise Survey Location (z/S) |
|---------------------|--------------------|-----------------------------|------------------------------|------------------------------|---|------------------------|--------------------------------|
| 2.5                 | 2.48               | 103.43                      | 6.27                         | 294                          | 10.08                                     | 75                     | 0.0777                         |
| 3.0                 | 2.93               | 120.57                      | 3.65                         | 298                          | 9.21                                      | 75                     | -0.040                         |
| 3.5                 | 3.48               | 241.05                      | 3.24                         | 298                          | 14.33                                     | 85                     | 0.0732                         |
| 4.0                 | 3.95               | 206.62                      | 1.45                         | 294                          | 9.82                                      | 125                    | 0.0622                         |
| 4.0                 | 3.95               | 206.62                      | 1.45                         | 294                          | 9.82                                      | 130                    | 0.0622                         |

Table 2. Wind Tunnel Model Instrumentation Locations

| Instrumentation Type  | Axial Position (cm) | Spanwise Position (cm) |
|-----------------------|---------------------|------------------------|
| Static Pressure Tap 1 | 3.81                | 0.0                    |
| Static Pressure Tap 2 | 9.53                | 7.62                   |
| Static Pressure Tap 3 | 13.97               | 7.62                   |
| Static Pressure Tap 4 | 18.42               | 7.62                   |
| Static Pressure Tap 5 | 25.4                | 0.0                    |
| Static Pressure Tap 6 | 30.48               | 0.0                    |
| Thermocouple          | 17.78               | -1.27                  |

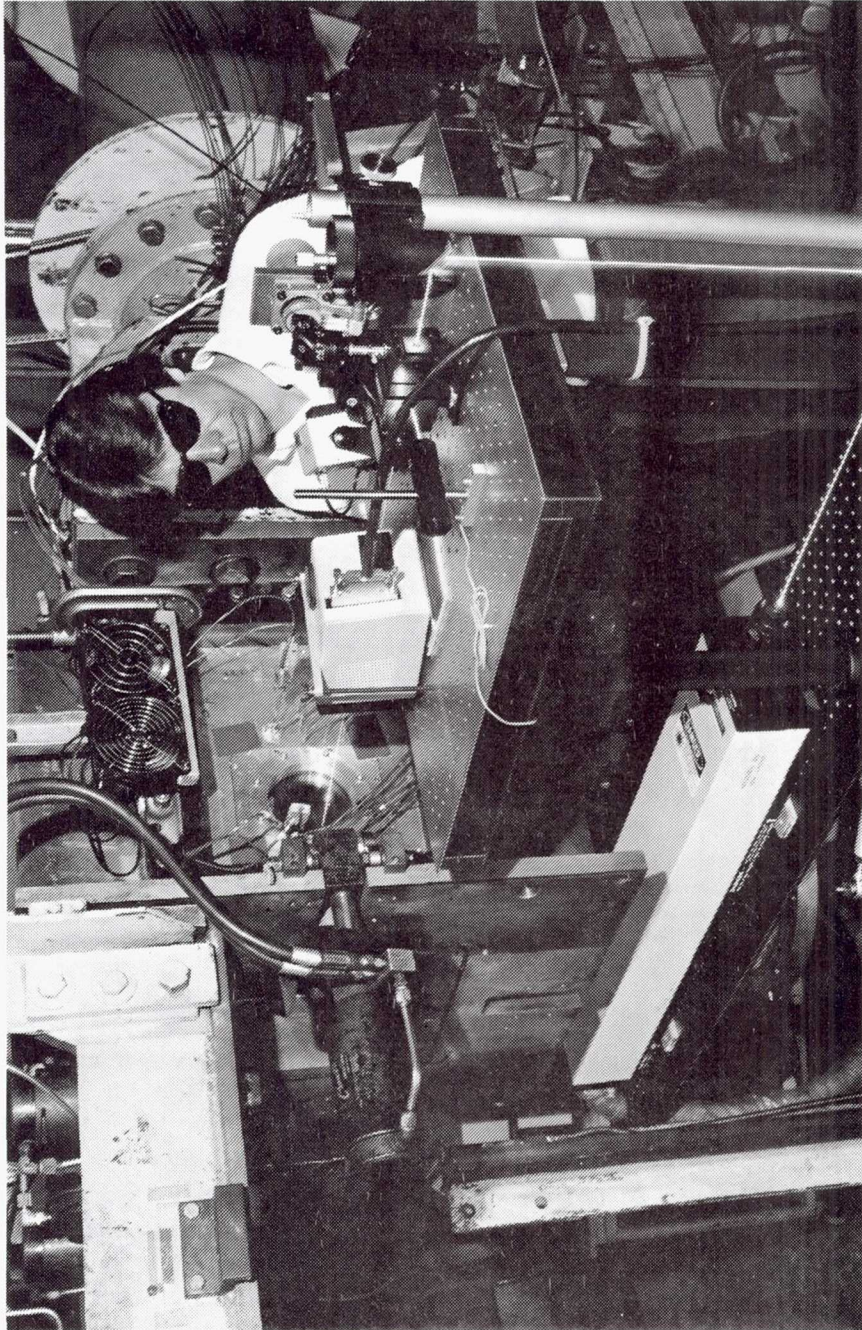


Figure 1. Photograph of LIHF System

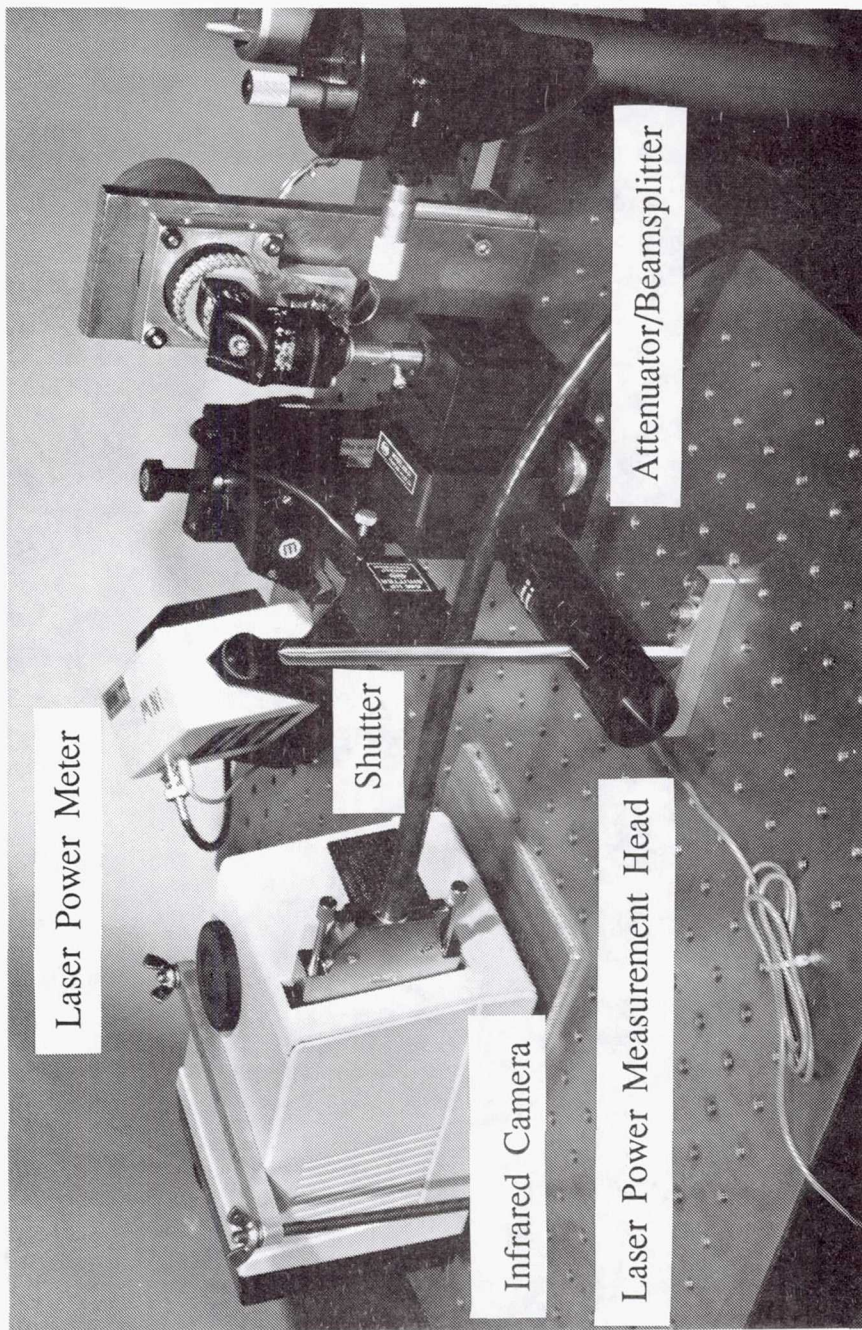


Figure 2. Close-up View of LIHF System

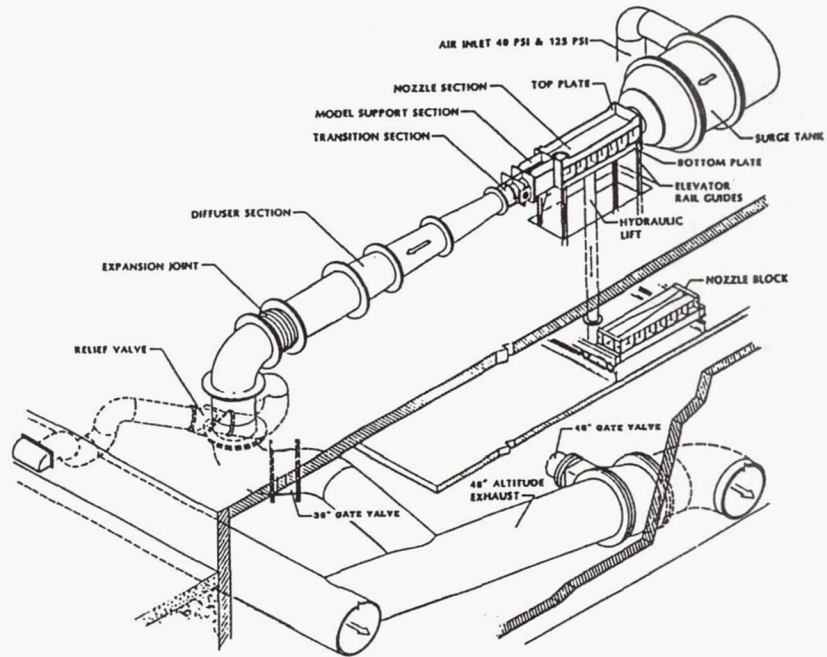


Figure 3. Schematic of NASA Lewis 1x1 Foot Supersonic Wind Tunnel

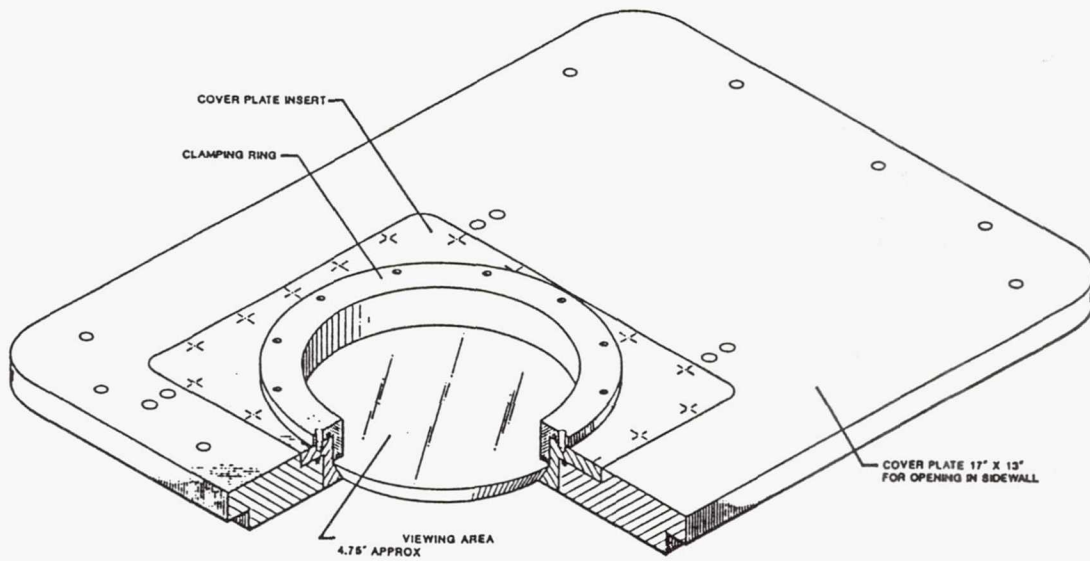


Figure 4. Schematic of Wind Tunnel Sidewall with Zinc Sulfide Window Insert

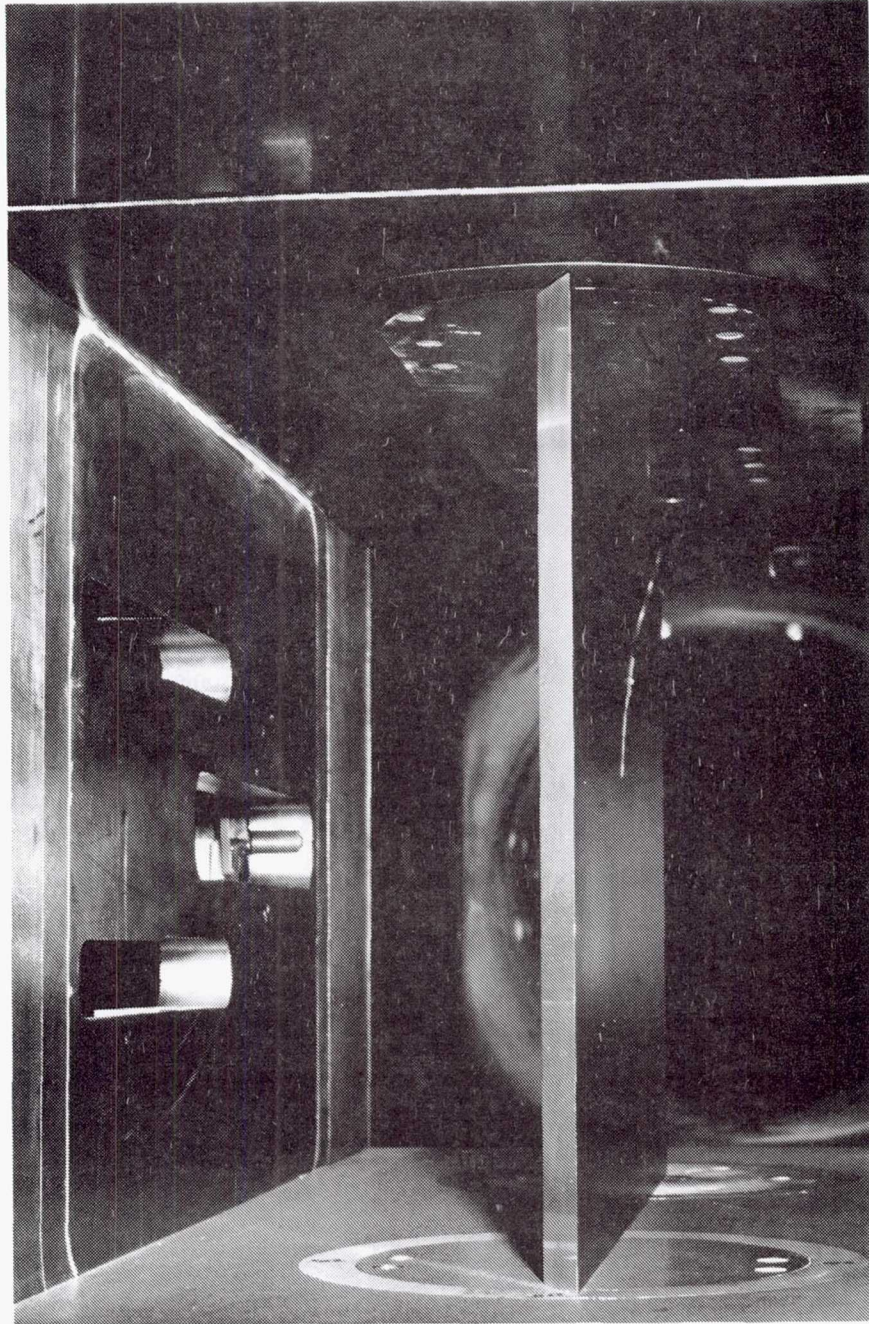


Figure 5. Photograph of Flat Plate Model Installed in NASA Lewis 1x1 SWT

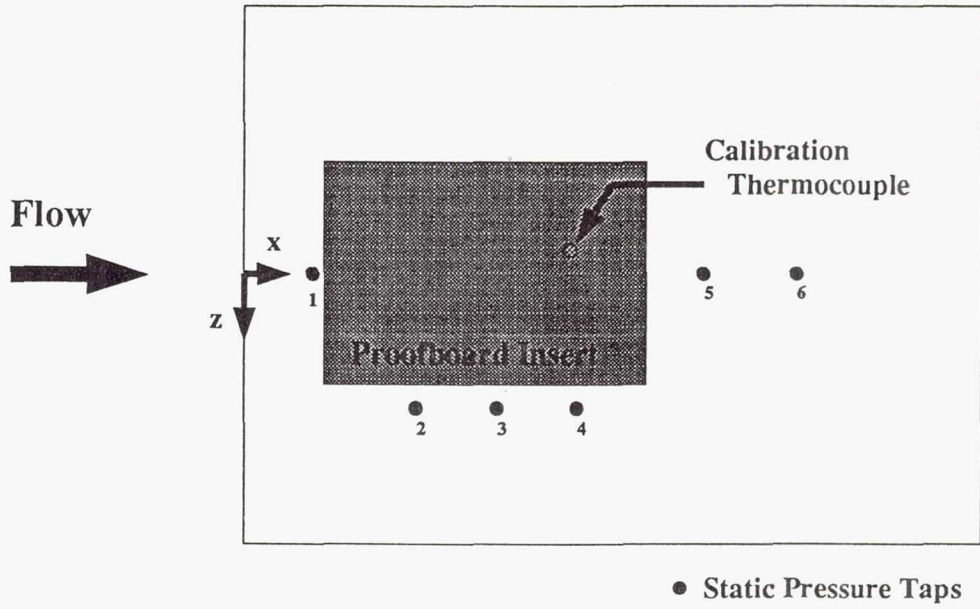


Figure 6. Schematic of Flat Plate Model

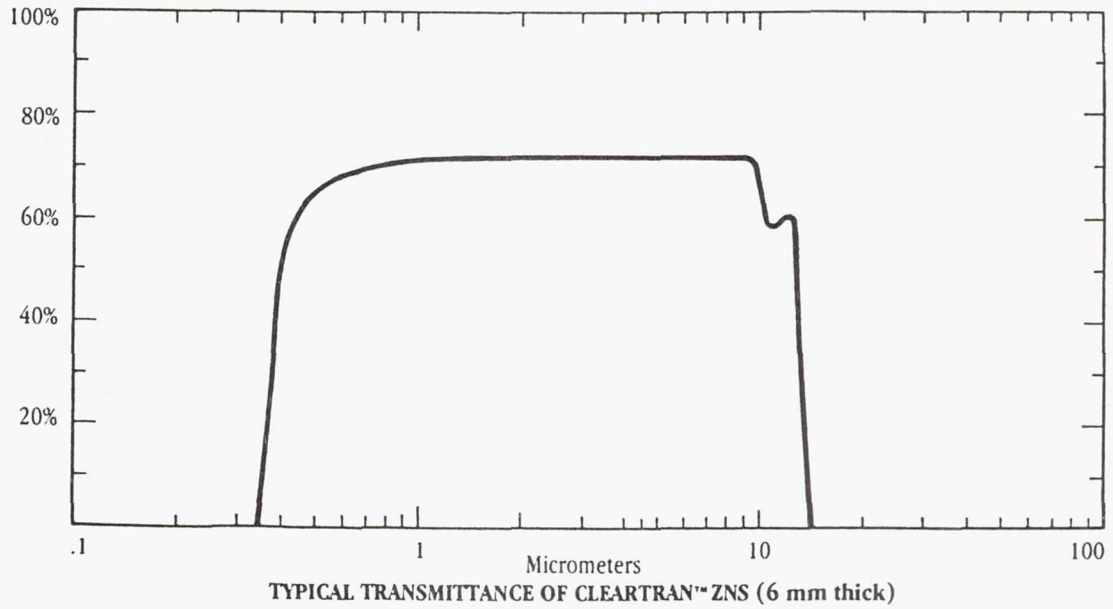


Figure 7. Energy Transmission Curve of CLEARTRAN Zinc Sulfide Material (from Ref. [19])

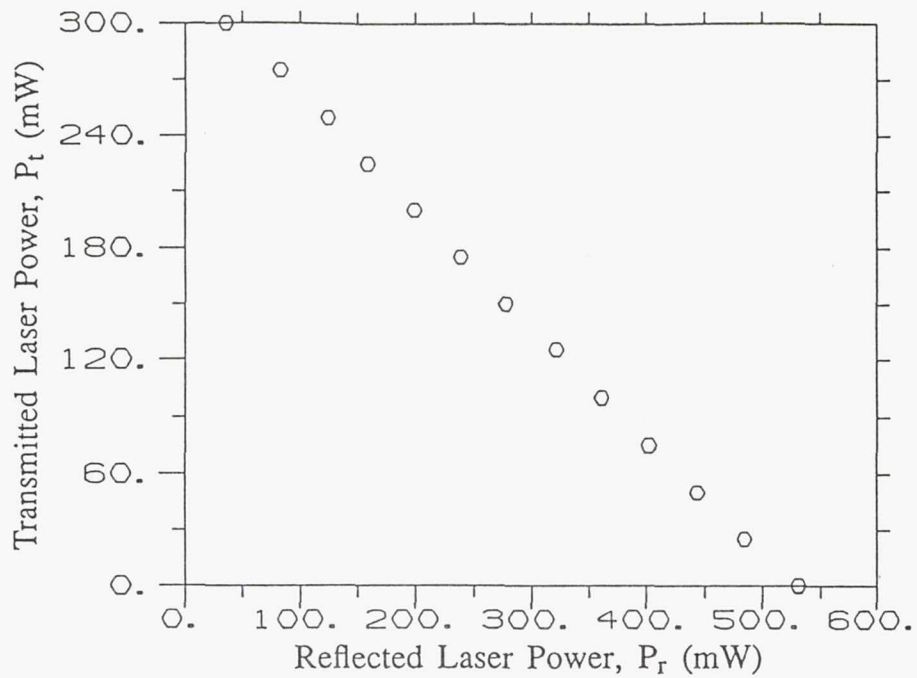


Figure 8. Typical Laser Power Calibration Curve

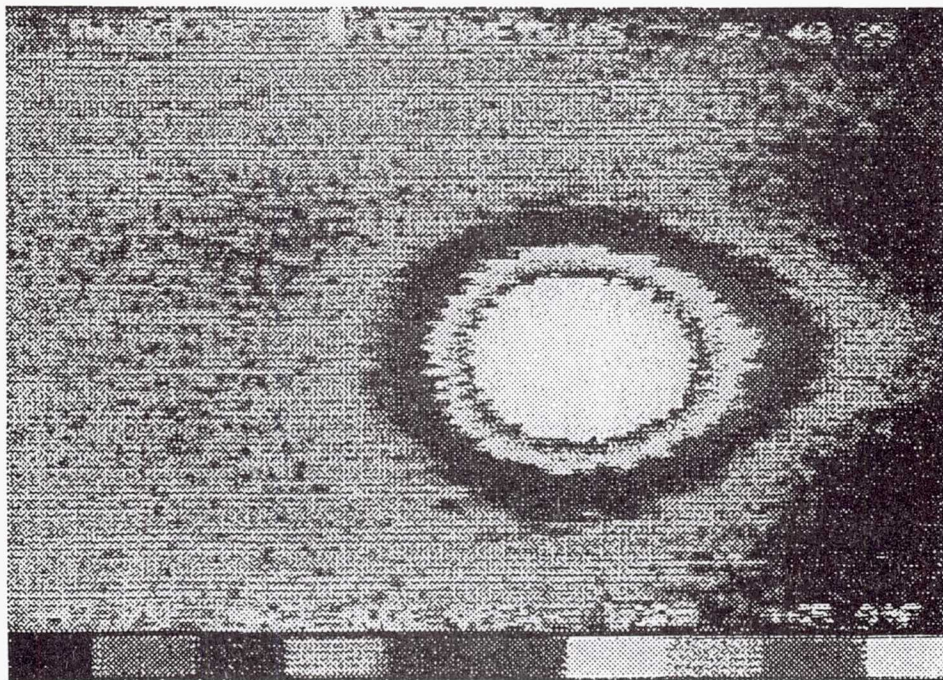


Figure 9. Typical Infrared Thermogram of Flow Surface Area Heated by Laser

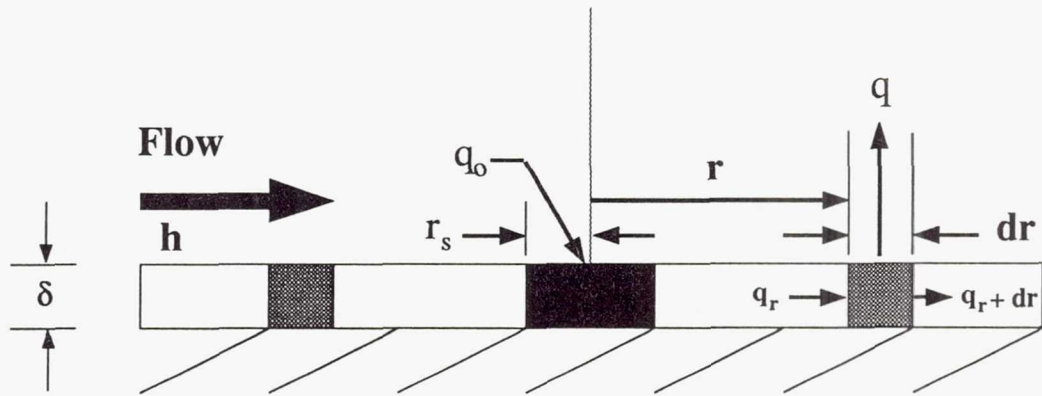


Figure 10. Cross-Sectional View of Flow Surface Measurement Region

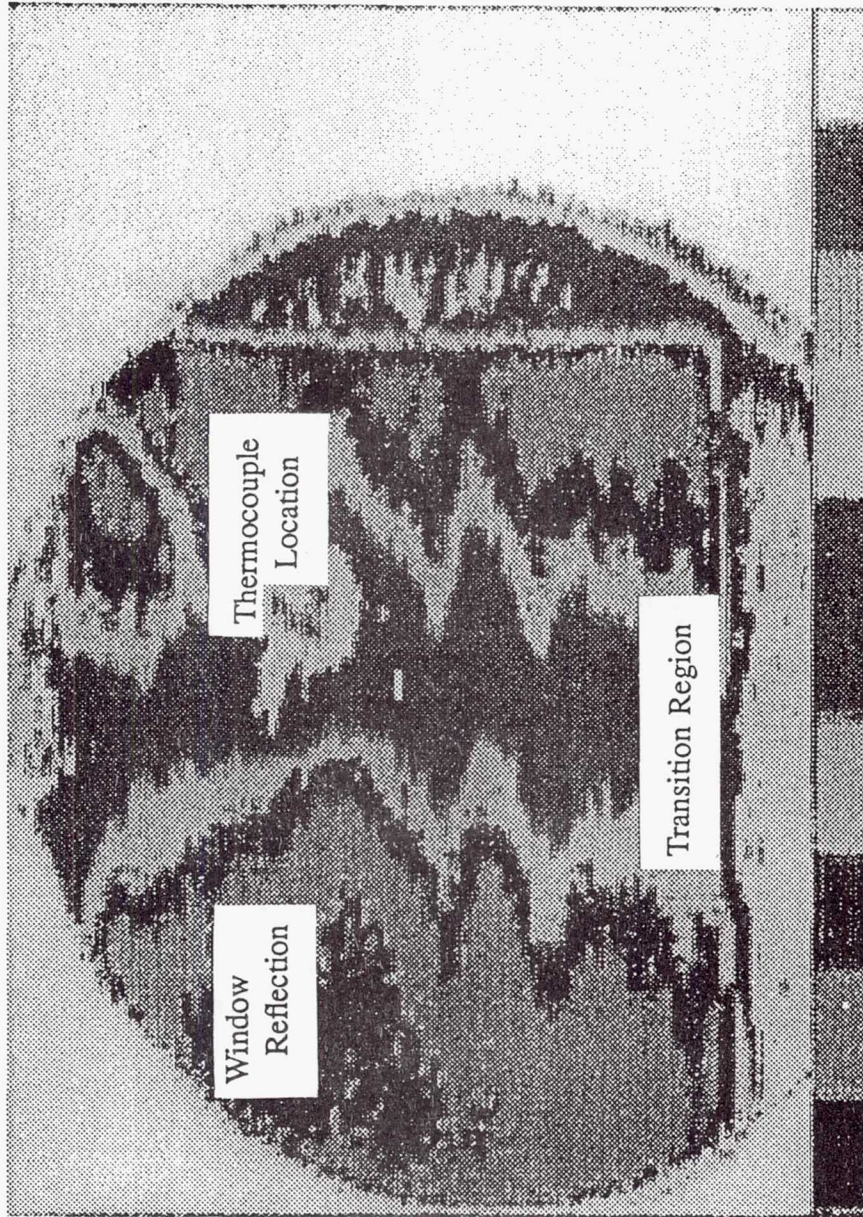


Figure 11. Overall Infrared Thermogram of Flow Surface,  $M_{\infty} = 4.0$

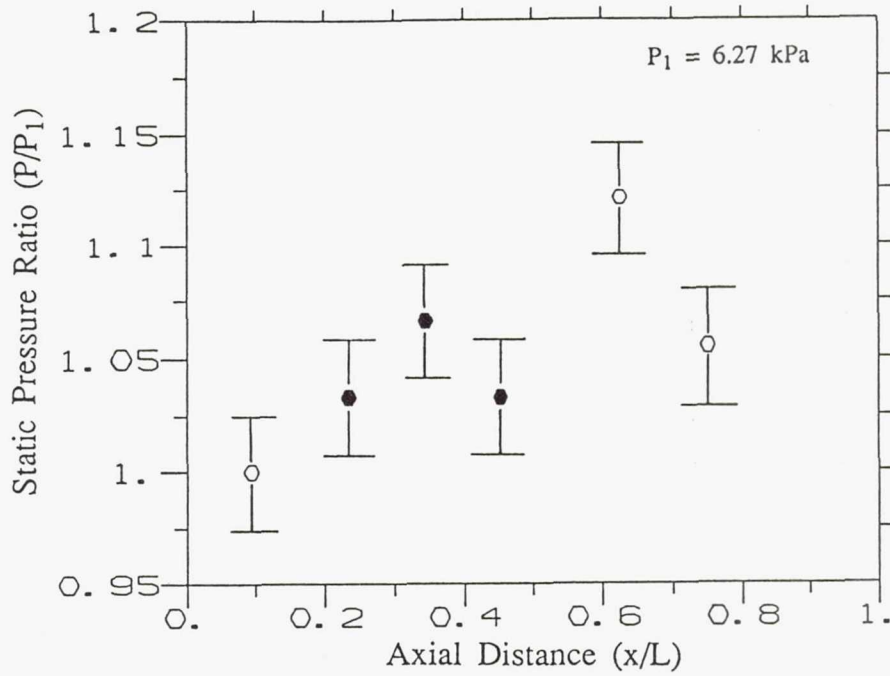


Figure 12. Flat Plate Static Pressure Distribution,  $M_\infty = 2.5$

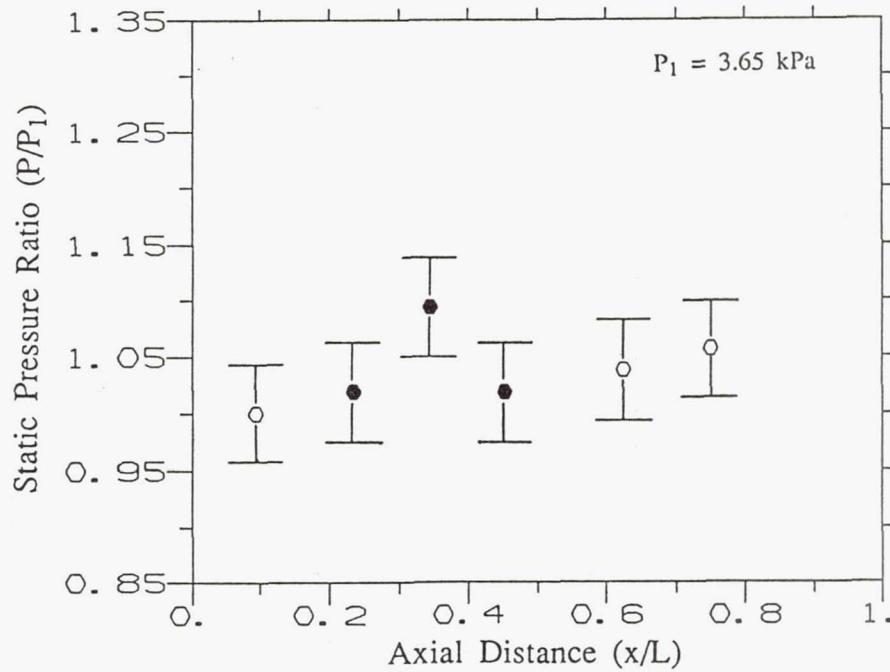


Figure 13. Flat Plate Static Pressure Distribution,  $M_\infty = 3.0$

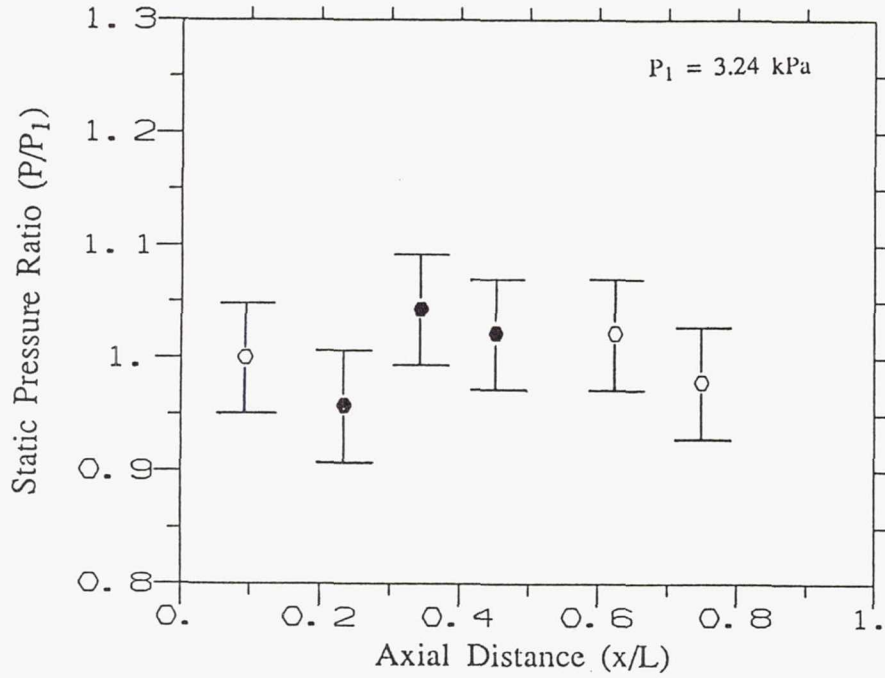


Figure 14. Flat Plate Static Pressure Distribution,  $M_\infty = 3.5$

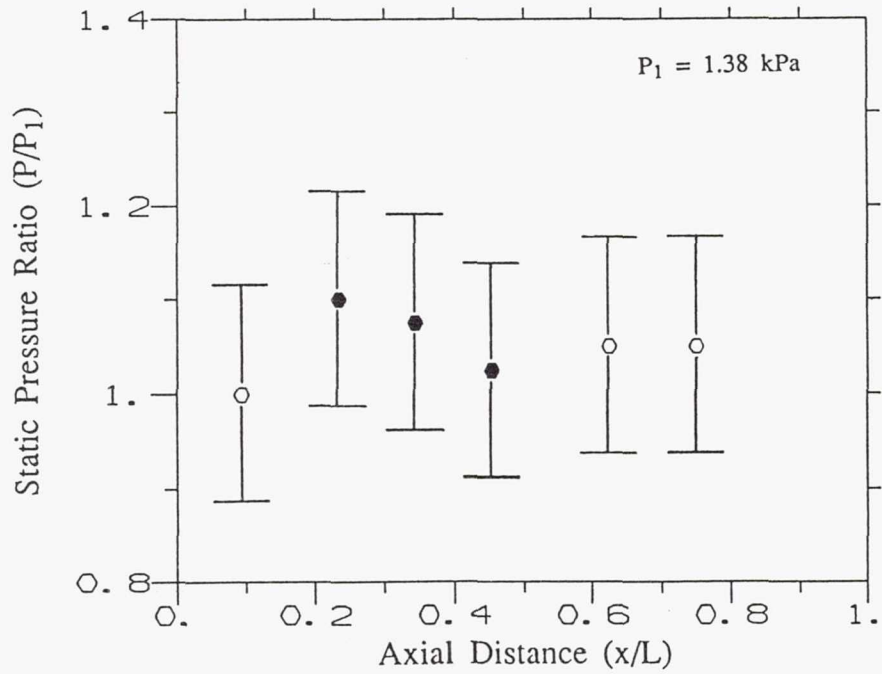


Figure 15. Flat Plate Static Pressure Distribution,  $M_\infty = 4.0$

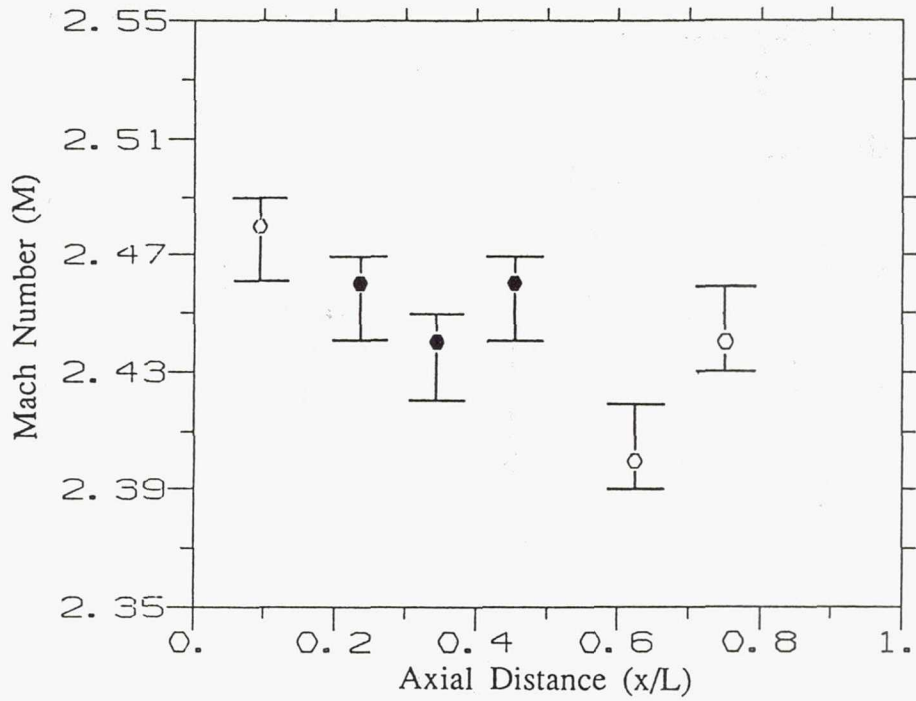


Figure 16. Flat Plate Local Mach Number Distribution,  $M_\infty = 2.5$

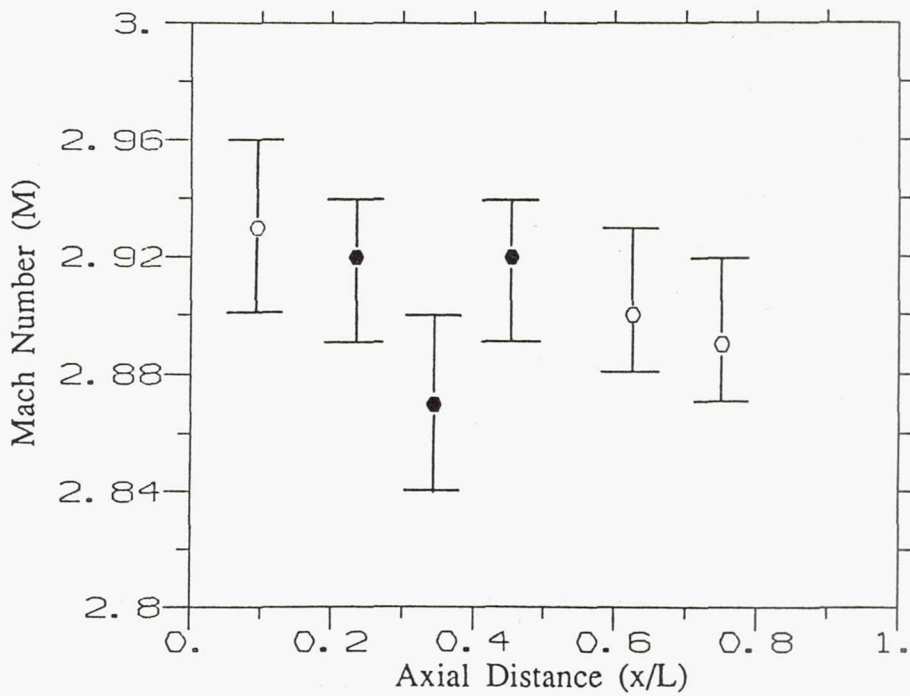


Figure 17. Flat Plate Local Mach Number Distribution,  $M_\infty = 3.0$

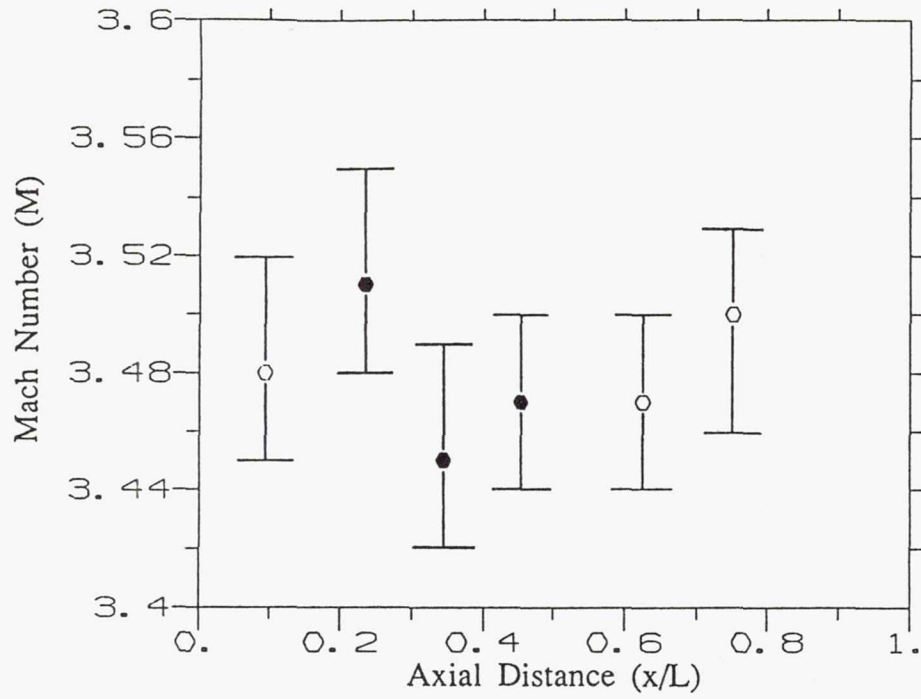


Figure 18. Flat Plate Local Mach Number Distribution,  $M_\infty = 3.5$

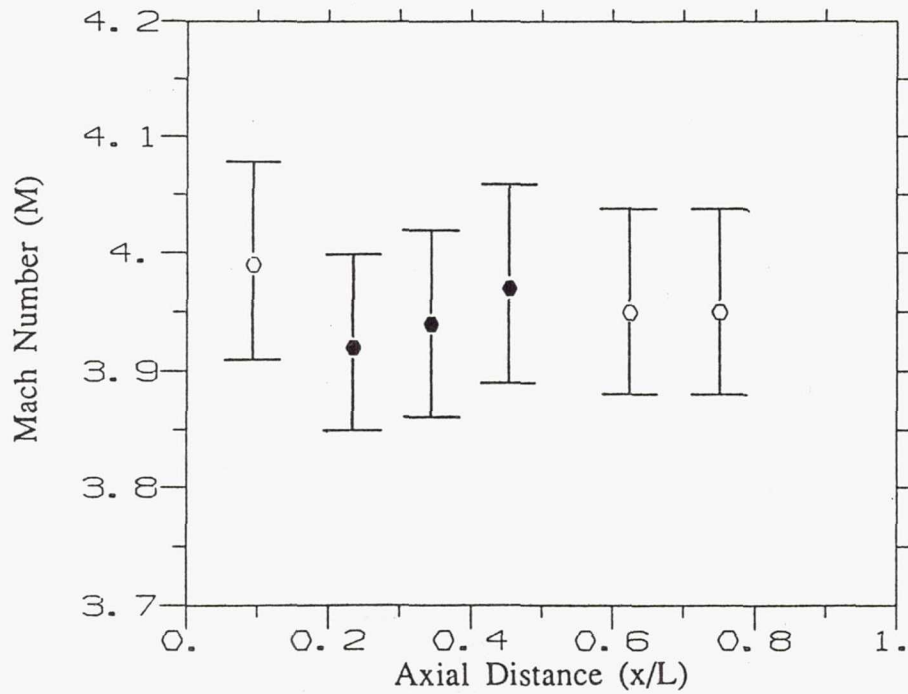


Figure 19. Flat Plate Local Mach Number Distribution,  $M_\infty = 4.0$

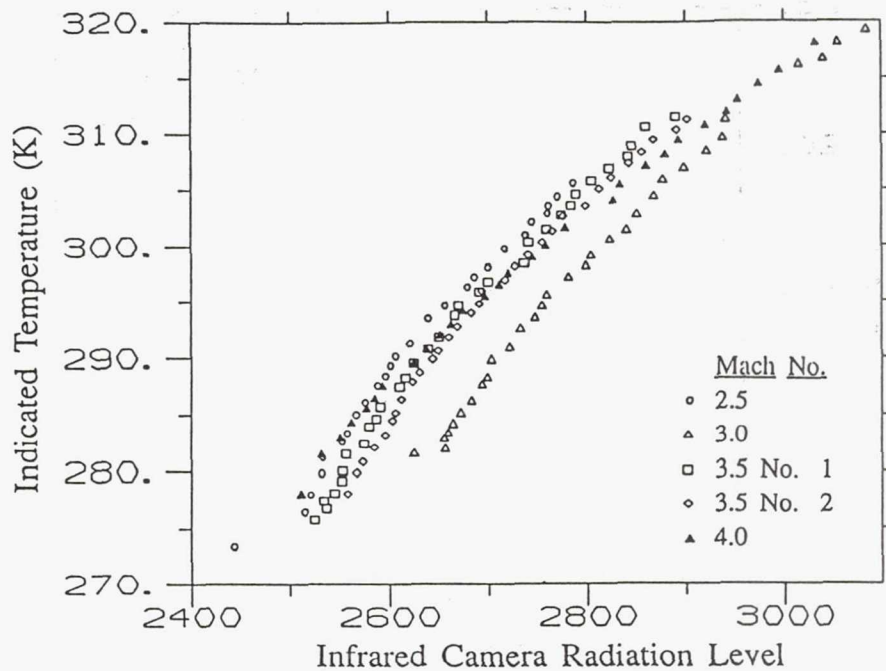


Figure 20. LIHF System Temperature Calibration Results

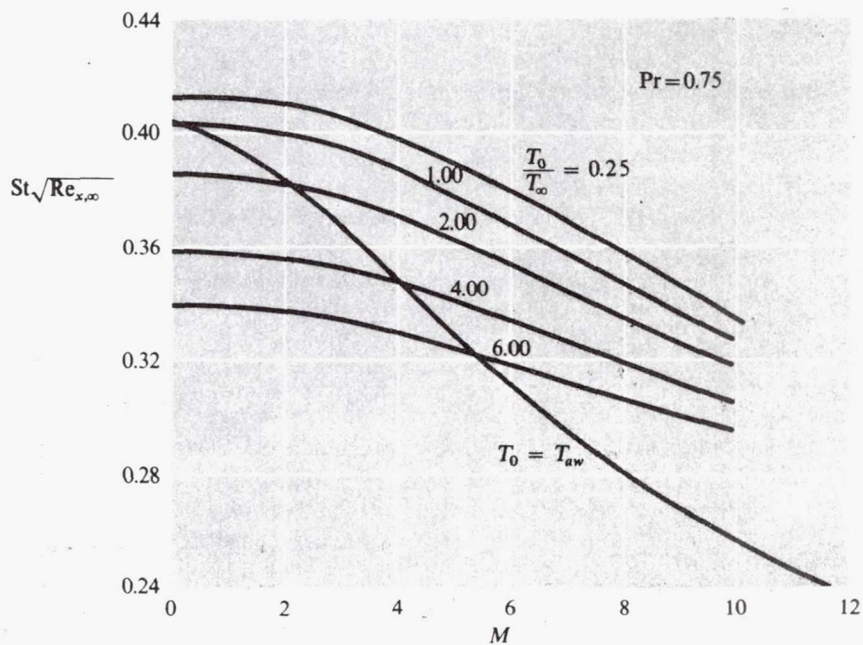


Figure 21. Theoretical Heat Transfer to or from the Laminar High Velocity Boundary Layer (from Ref. [22])

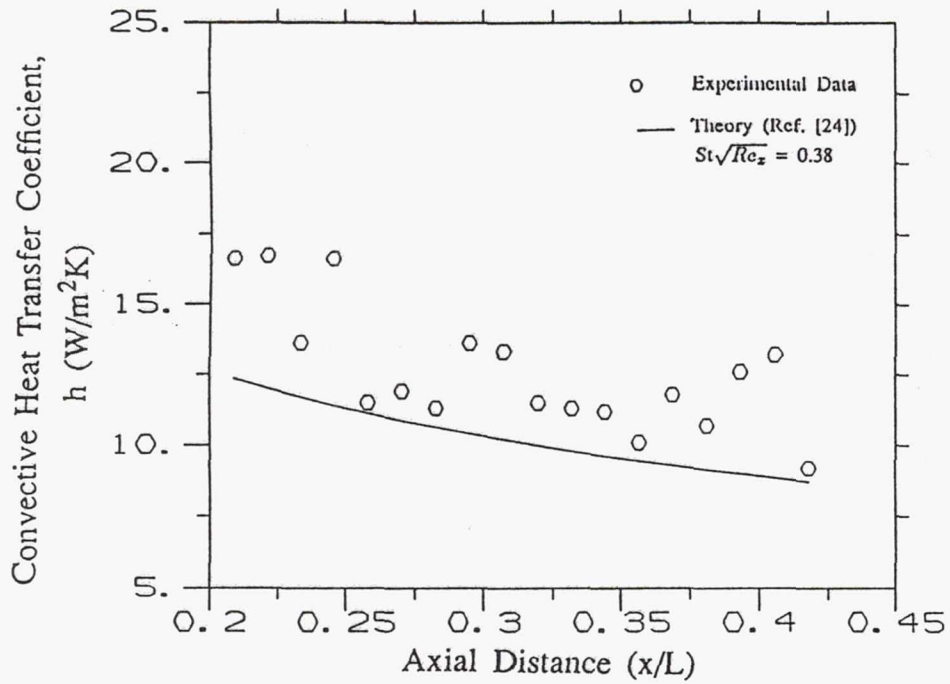


Figure 22. Flat Plate Convective Heat Transfer Coefficient Distribution,  $M_\infty = 2.5$

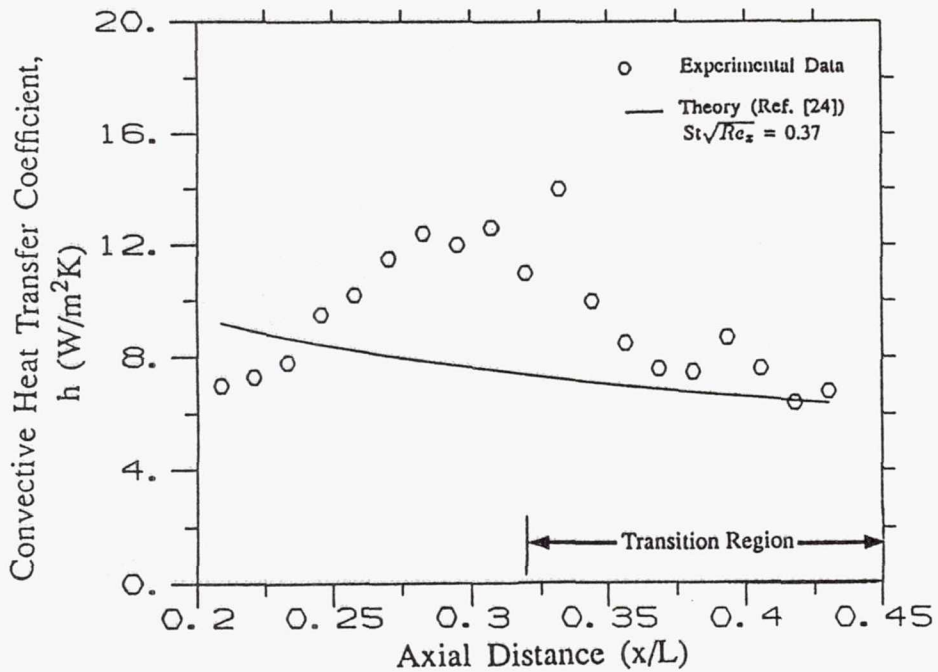
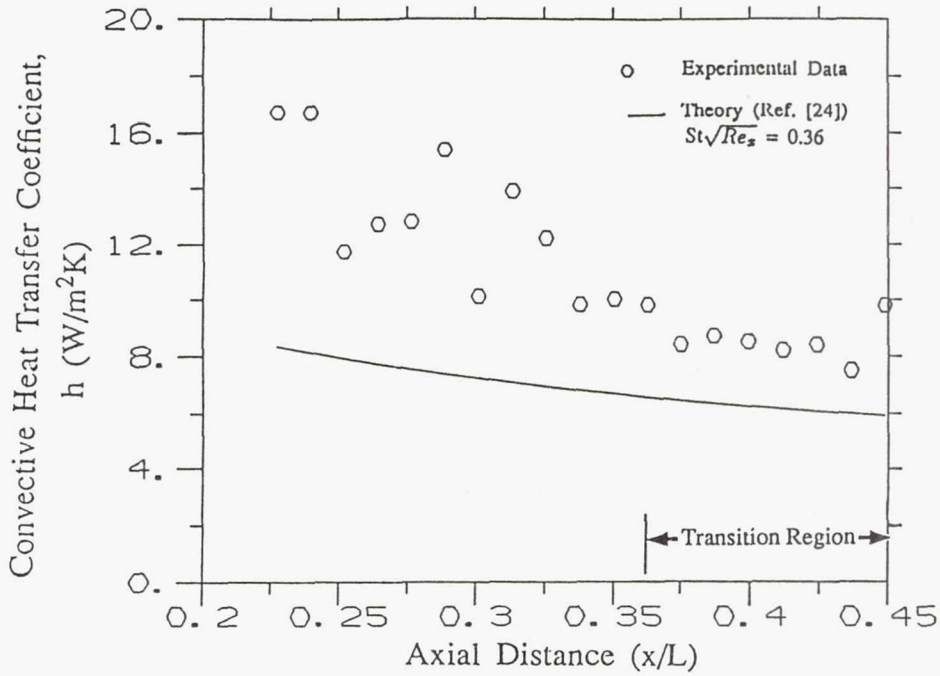
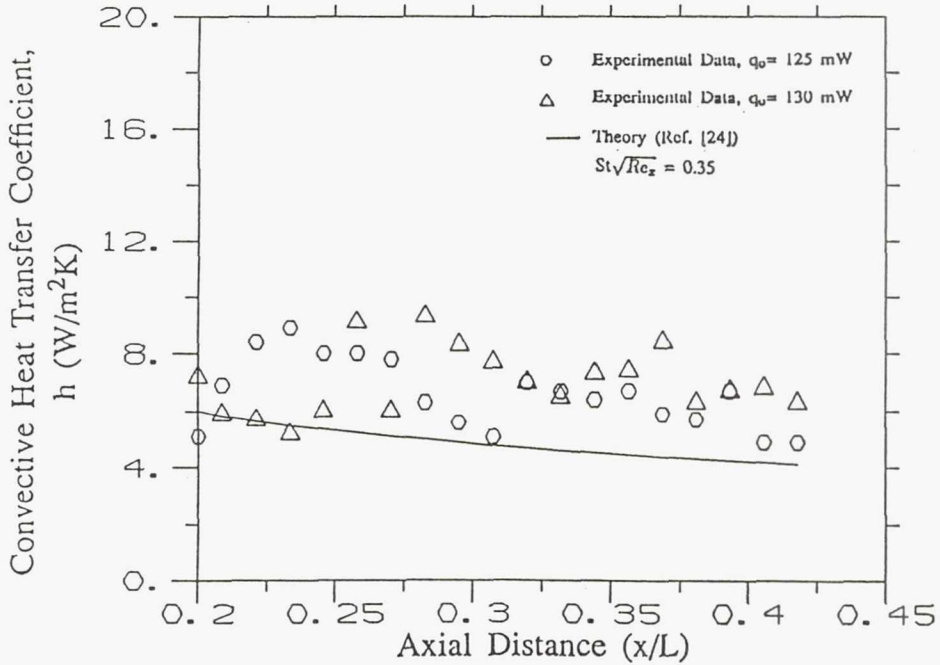


Figure 23. Flat Plate Convective Heat Transfer Coefficient Distribution,  $M_\infty = 3.0$

Figure 24. Flat Plate Convective Heat Transfer Coefficient Distribution,  $M_\infty = 3.5$ Figure 25. Flat Plate Convective Heat Transfer Coefficient Distribution,  $M_\infty = 4.0$



National Aeronautics and  
Space Administration

## Report Documentation Page

|  |  |  |  |   |                   |
|--|--|--|--|---|-------------------|
| 1. Report No.<br>NASA TM-103778  |  | 2. Government Accession No.                          |  | 3. Recipient's Catalog No.                                    |                   |
| 4. Title and Subtitle<br>Development of a Laser-Induced Heat Flux<br>Technique for Measurement of Convective Heat<br>Transfer Coefficients in a Supersonic Flowfield   |  |  |  | 5. Report Date<br>March 1991                                  |                   |
|  |  |  |  | 6. Performing Organization Code                               |                   |
| 7. Author(s)<br>A. Robert Porro, Theo G. Keith, Jr., Warren R. Hingst, Randall M. Chriss,<br>and Kirk D. Seablom   |  |  |  | 8. Performing Organization Report No.<br>E-6049               |                   |
|  |  |  |  | 10. Work Unit No.<br>505-62-52                                |                   |
| 9. Performing Organization Name and Address<br>National Aeronautics and Space Administration<br>Lewis Research Center<br>Cleveland, Ohio 44135-3191  |  |  |  | 11. Contract or Grant No.                                     |                   |
|  |  |  |  | 13. Type of Report and Period Covered<br>Technical Memorandum |                   |
| 12. Sponsoring Agency Name and Address<br>National Aeronautics and Space Administration<br>Washington, D.C. 20546-0001   |  |  |  | 14. Sponsoring Agency Code                                    |                   |
|  |  |  |  |   |                   |
| 15. Supplementary Notes<br>A. Robert Porro, Warren R. Hingst, Randall M. Chriss, and Kirk D. Seablom, NASA Lewis Research Center;<br>Theo G. Keith, Jr., University of Toledo, Toledo, Ohio 43606. Responsible person, A. Robert Porro, (216) 433-5921.  |  |  |  |   |                   |
| 16. Abstract<br>In this study, a technique is developed to measure the local convective heat transfer coefficient on a model surface in a supersonic flowfield. The technique uses a laser to apply a discrete local heat flux at the model test surface, and an infrared camera system determines the local temperature distribution due to the heating. From this temperature distribution and an analysis of the heating process, a local convective heat transfer coefficient is determined. The technique was used to measure the local surface convective heat transfer coefficient distribution on a flat plate at nominal Mach numbers of 2.5, 3.0, 3.5, and 4.0. The flat plate boundary layer initially was laminar and became transitional in the measurement region. The experimental results agreed reasonably well with theoretical predictions of convective heat transfer of flat plate laminar boundary layers. The results indicate that this non-intrusive optical measurement technique has the potential to obtain high quality surface convective heat transfer measurements in high speed flowfields. |  |  |  |   |                   |
| 17. Key Words (Suggested by Author(s))<br>Convective heat transfer<br>Boundary layers  |  |  | 18. Distribution Statement<br>Unclassified - Unlimited<br>Subject Categories 02 and 34 |   |                   |
| 19. Security Classif. (of the report)<br>Unclassified  |  | 20. Security Classif. (of this page)<br>Unclassified |  | 21. No. of pages<br>56  | 22. Price*<br>A04 |